A Multiscale Reexamination of the Pacific–South American Pattern

TERENCE J. O'KANE, DIDIER P. MONSELESAN, AND JAMES S. RISBEY

CSIRO Oceans and Atmosphere, Hobart, Australia

(Manuscript received 29 July 2016, in final form 5 October 2016)

ABSTRACT

The authors undertake a multiscale spectral reexamination of the variability of the Pacific–South American (PSA) pattern and the mechanisms by which this variability occurs. Time scales from synoptic to interannual are investigated, focusing on the means by which tropical variability is communicated to the midlatitudes and on in situ forcing within the midlatitude waveguides. Particular interest is paid to what fraction of the total variability associated with the PSA, occurring on interannual time scales, is attributable to tropical forcing relative to that occurring on synoptic and intraseasonal time scales via internal waveguide dynamics. In general, it is found that the eastward-propagating wave train pattern typically associated with the PSA manifests across time scales from synoptic to interannual, with the majority of the variability occurring on synoptic-to-intraseasonal time scales largely independent of tropical convection. It is found that the small fraction of the total variance with a tropical signal occurs via the zonal component of the thermal wind modulating both the subtropical and polar jets. The respective roles of the Hadley circulation and stationary Rossby wave sources are also examined. Further, a *PSA-like* mode is identified in terms of the slow components of higher-order modes of tropospheric geopotential height. This study reestablishes the multiscale nonlinear nature of the PSA modes arising largely as a manifestation of internal midlatitude waveguide dynamics and local disturbances.

1. Introduction

Many mechanisms have been invoked to explain the modulation of persistent circulation patterns in the South Pacific. These include direct processes, such as tropical convection and Rossby wave sources associated with El Niño–Southern Oscillation (ENSO) (Karoly 1989; Renwick and Revell 1999; Cai et al. 2011) and the Madden–Julian oscillation (MJO) (Mo and Paegle 2001; Hirata and Grimm 2016), to more indirect modulation of the subtropical and polar jets in response to changes in the Hadley circulation (Hu and Fu 2007; Freitas and Ambrizzi 2012; Nguyen et al. 2013; Freitas et al. 2016) or by the thermal winds (Reid and Gage 1984; Dickey and Marcus 1992; Mo et al. 1997). Alternately, local drivers such as the resonant interaction between Rossby waves, flow instabilities, and the internal dynamics of the jets have been invoked [see O'Kane et al. (2016b) and references therein]. While undoubtedly multiple processes play a role, even a cursory reading of the literature indicates there is a considerable degree of disagreement as to the relative importance of each, particularly on time scales from intraseasonal to interannual.

The now standard interpretation of an empirical orthogonal function (EOF)/principal component (PC) analysis (Lorenz 1956; Hannachi et al. 2007) of Southern Hemisphere (SH) 500-hPa geopotential height anomalies ($Z_g^{500\mathrm{hPa}}$) is that the leading mode EOF1 pattern, showing a strong zonal symmetry at high latitudes, and a zonal wavenumber-3 structure with centers located in the Indian, Pacific, and Atlantic southern oceans, defines the southern annular mode (SAM) (Rogers and van Loon 1982; Szeredi and Karoly 1987; Thompson and Wallace 2000). Since the early papers of Karoly (1989) and Ghil and Mo (1991), it has been recognized that SH circulation features in the South Pacific are, on interannual time scales, highly correlated with ENSO. Lau et al. (1994) described the EOFs 2 and 3 patterns of $Z_g^{500\mathrm{hPa}}$ as the Pacific–South American (PSA) modes PSA1 and PSA2, characterizing them as well-defined wave trains (wave 4) extending from southeastern Australia to Argentina whose centers are located at 60°S, 120°W (PSA1) and 60°S, 90°W (PSA2), respectively. Mo (2000) alternately describes these modes as representing a wavenumber-3 pattern from the tropical

Corresponding author e-mail: Terence J. O'Kane, terence.okane@csiro.au

DOI: 10.1175/MWR-D-16-0291.1

Pacific to Argentina, with large amplitudes in the Pacific–South American sector. They associate the PSA1, on interannual time scales, with the low-frequency part of ENSO variability and a dominant period of 40–48 months; whereas the PSA2 mode is associated with the quasi-biennial component of ENSO variability and a period of 26 months.

On time scales from a few days to about a month, it has for some time now been posited that atmospheric blocking events over the South Pacific could also be strongly modulated by the ENSO cycle, particularly during austral spring and summer. Renwick and Revell (1999) examined 30-day low-pass-filtered $Z_g^{500\mathrm{hPa}}$ anomalies and the 300-hPa meridional wind component, finding that persistent SH blocking events were also associated with large-scale wave trains lying across the South Pacific from the region of Australia to southern South America. Renwick (2005) applied *k*-means clustering to $Z_g^{500\mathrm{hPa}}$ anomalies and a strong blocking criteria (at least 100 m in magnitude lasting for at least 5 days), identifying the southeast Pacific near 60°S and a hemispheric zonal wavenumber-3 pattern as the regions where persistent positive anomalies occur. Only the southeast Pacific was found to be modulated by ENSO. The progression of these blocking events from onset to decay shows patterns consistent with the PSA modes.

In a broader sense, dynamical mode theory produces classes of intermediate scale and period modes—on the intraseasonal time scale—which, apart from the tropical signal of the MJO, have been little studied based on observations. Frederiksen and Lin (2013) describe how these intermediate scale and period modes have extratropical structures quite similar to the major Pacific–North American (PNA) and North Atlantic Oscillation (NAO) teleconnection patterns (i.e., dipolar patterns of low-frequency tropospheric height variability manifesting in the North Pacific and North Atlantic sectors of the Northern Hemisphere). In the case of the PSA, the leading dynamical mode is an instability that has an intraseasonal period (22 days) (Frederiksen and Frederiksen 1993), which is consistent with the earlier findings of Lau et al. (1994).

O'Kane et al. (2013) investigated systematic changes (secular trends) and regime behavior (frequency of occurrence and persistence) in the SH tropospheric circulation in terms of blocking, planetary wavenumber-3, and the respective phases of the SAM via application of data driven nonparametric cluster analysis. O'Kane et al. (2016b) extended this approach to reveal the secular behavior of the PSA pattern and blocking modes over recent decades. They found the PSA exhibited significant variations on interannual-to-decadal time scales. However, consistent with the study of South Pacific winter blocking by Oliveira et al. (2014), no large systematic linear trends were identified in the region upstream of South America. The studies of O'Kane et al. (2013, 2016b) found resonant interactions between local disturbances and local stationary Rossby wave sources within the SH midlatitude subtropical and polar jets to be the dominant mechanism by which coherent structures, such as blocking and the PSA, form (i.e., extratropical internal dynamics on synoptic-to-intraseasonal time scales).

The alternative interpretation to the instability paradigm is one in terms of stationary Rossby waves in a stable background flow generated via a sustained source (up to 16 days), usually tropical SST anomalies of several degrees (Hoskins and Karoly 1981; Karoly 1983; Branstator 1983; Hoskins and Ambrizzi 1993; Renwick and Revell 1999). Based on Wentzel–Kramers–Brillouin (WKB) and ray tracing theory, Hoskins and coworkers (Hoskins and Ambrizzi 1993; Ambrizzi et al. 1995; Jin and Hoskins 1995; Ambrizzi and Hoskins 1997) articulated the role of the subtropical and polar jet streams as waveguides for stationary Rossby wave activity. These studies, and in particular the one of Karoly (1983), were highly influential on later studies of the PSA such as the one by Mo and Paegle (2001) where the low-frequency variability of the PSA1 is attributed to stationary Rossby waves generated via large-amplitude tropical SST anomalies (SSTAs) in response to ENSO. On synoptic time scales, Renwick and Revell (1999) hypothesized that the divergence associated with tropical outgoing longwave radiation anomalies forces an extratropical wave response resulting in enhanced blocking over the southeast Pacific. They argue that linear Rossby wave propagation provides the link between anomalous convection in the tropics and the occurrence of blocking over the southeast Pacific Ocean.

Many recent studies, of which the one of Cai et al. (2011) is characteristic, have continued to invoke the aforementioned early examinations of stationary Rossby wave propagation to explain the influence of tropical forcing on midlatitude dynamics, often without sufficient regard for the seasonally dependent barriers to stationary Rossby wave propagation of the type identified by Ambrizzi et al. (1995) and more recently reexamined by Li et al. (2015). In particular, it is well known from ray tracing theory that, coincident with the establishment of the subtropical jet in the austral winter, Rossby wave propagation from the tropics to the midlatitudes in the South Pacific is largely blocked by the establishment of a reflecting surface poleward of the subtropical jet east of 60°E and west of 120°W (Hoskins and Karoly 1981; Hoskins and Ambrizzi 1993; Ambrizzi et al. 1995; Ambrizzi and Hoskins 1997;

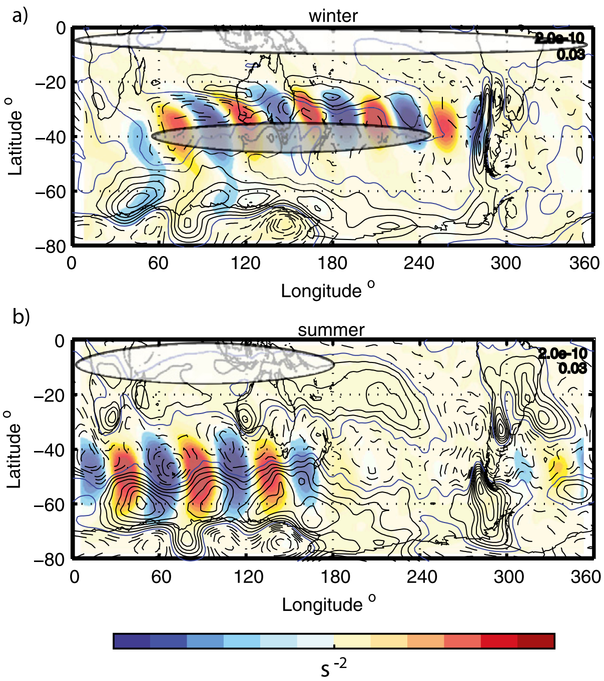

FIG. 1. Climatological Rossby wave source values (contours) and the leading EOF pattern of Rossby wave source (shaded) calculated from daily anomalies w.r.t. the climatological mean for (a) winter and (b) summer. The range of values is indicated in the top right of each panel with contours uppermost and shaded below. Approximate regions where Rossby wave breaking occurs (O'Kane et al. 2016b) in the tropics are indicated by the white ellipses, whereas the region where a reflective barrier to Rossby wave propagation forms, with maximum extent in the austral winter, is indicated by the gray ellipse. The colors and intervals of the color bar are scaled to min–max values indicated by their corresponding absolute value in the top right hand of each panel (contour absolute value at top, shading below).

Li et al. 2015). This surface occurs where the total wavenumber is imaginary due to a negative meridional gradient of vorticity (see schematic in Fig. 1). This barrier represents a major problem for studies that invoke the excitation of equivalent barotropic Rossby wave trains propagating from the tropics into the extratropics, initiated by diabatic heating anomalies in the tropical equatorial Pacific during the austral autumn, winter, and or spring, as an explanation for the establishment of the PSA pattern and even blocking in the southeast Pacific (Karoly 1989). That said, Jin and Hoskins (1995) showed that, during the austral summer (December–February), anomalous divergence over the Maritime Continent imposed on the background state could lead to the excitation of stationary Rossby wave trains that propagate into the SH in the absence of the subtropical jet. The schematic in Fig. 9 of Cai et al. (2011) is the canonical representation of much current thinking about the role of tropical–extratropical wave trains associated with the PSA, largely based on the ENSO mechanism of Karoly (1989).

There is a growing body of literature regarding the influence of both ENSO and global warming on the zonal mean Hadley circulation. In particular global warming has been shown to lead to a general expansion of the tropical circulation (Lu et al. 2007; Vecchi and Soden 2007; Lu et al. 2009), whereas it has been argued that during strong El Niño events there is a corresponding contraction of the Hadley circulation (Hu and Fu 2007; Freitas and Ambrizzi 2012; Nguyen et al. 2013; Freitas et al. 2016).

The role of the stationary Rossby waves and the internal dynamics of the subtropical and polar jets on the frequency and duration of persistent patterns in SH has been the subject of detailed studies by O'Kane et al. [2013, 2016a (manuscript submitted to *Climate Dyn.*), 2016b]. Here we focus on midlatitude SH tropospheric variability with a particular focus on that part of the variability that is highly correlated with ENSO. To this end, we consider Z_g, zonal mean meridional mass streamfunction ψ^{mms}, air temperature at the surface and at 500 hPa, and thermal wind, all taken from the Japanese 55-year Reanalysis (JRA-55) reanalysis over the period 1958 to 2013. Here EOF/PC analysis is applied largely as a tool to reduce the dimensionality of the task. We then apply singular spectral analysis (SSA) (Elsner and Tsonis 1996; Ghil et al. 2002; Golyandina and Zhigljavsky 2013) to the leading PCs as a means of analyzing the multiple time scales of the particular circulation modes. This approach is similar to the earlier studies of Ghil and Mo (1991), Lau et al. (1994), and Mo (2000). However, unlike most previous studies of the PSA modes, we do not prefilter the daily data in any way before calculating the leading EOF patterns and their PCs. Correlation with the original anomaly time series is employed to ascertain the spatial patterns of the respective SSA-reconstructed components.

Here we are interested to see how changes in the tropical circulation might modulate persistent circulation patterns in the extratropical Pacific via changes in the Hadley circulation (Freitas and Ambrizzi 2012). We also investigate the influence of the thermal winds on the South Pacific tropospheric circulation via coherent interannual fluctuations in atmospheric angular momentum associated with the ENSO cycle (Reid and Gage 1984; Dickey and Marcus 1992; Mo et al. 1997). Correlation with the multivariate ENSO index (MEI) is employed to indicate tropical Pacific influences. We are particularly motivated to ascertain what fraction of variance described by the SSA-reconstructed components is highly correlated with ENSO in each of the respective PSA modes.

Identifying the mechanisms by which the PSA occurs has important consequences for understanding its effect on the high latitudes of the South Pacific. Recent studies of temperature and precipitation variability over West Antarctica and the Antarctic Peninsula (Ding et al. 2011; Schneider et al. 2012; Steig et al. 2012; Ding and Steig 2013; Clem and Fogt 2015) and on sea ice variability in the adjacent Amundsen, Bellingshausen, and Weddell Seas [Matear et al. (2015) and references therein] have been linked to the low-frequency circulation variations due to PSA variability and modulated by anomalous tropical Pacific sea surface temperatures due to ENSO. It is noticeable that in the recent study of ERA-Interim data by Irving and Simmonds (2016), while confirming that the PSA pattern does indeed have a strong influence on observed warming over the Antarctic Peninsula during the austral autumn, they find only a very weak relationship between PSA variability and ENSO.

The data and diagnostics are described in section 2. Section 3 contains results of the EOF/PC analysis and multiscale spectral analysis of geopotential height, the Hadley circulation, as well as air temperature and thermal wind anomalies. Section 4 contains the conclusions. Details of the SSA are presented in the appendix.

2. Data and diagnostics

To examine the dynamics of the troposphere, we consider geopotential height on the $Z_g^{300\mathrm{hPa}}$-, $Z_g^{500\mathrm{hPa}}$-, and $Z_g^{700\mathrm{hPa}}$-m isobaric pressure surfaces, surface air temperature (SAT), temperature at 500 hPa ($T^{500\mathrm{hPa}}$), zonal mean meridional mass streamfunction ψ^{mms}, and thermal winds ($\mathbf{v}_T$) for daily mean data. All data are taken from the JRA-55 conducted by the Japan Meteorological Agency (JMA) (Kobayashi et al. 2015), which spans the global radiosonde period from 1958. We also note that our analyses of 500 geopotential height empirical modes and spectra from the ECMWF twentieth-century reanalysis (ERA-20C) and NOAA (20C and v1) reanalyses are broadly consistent with those reported for the JRA-55.

Commonly used to quantify airmass transport across meridians, the zonal mean meridional mass streamfunction (Oort and Yienger 1996) is defined as

$$\psi^{\mathrm{mms}}(\phi,p,t)=\frac{2\pi a\cos\phi}{g}\int_p^{p_s} v(p',\phi,t)\,dp', \qquad (1)$$

where a is Earth's radius, ϕ is the latitude, $v(p', \phi, t)$ is the zonally averaged meridional velocity, p is the pressure, p_s is pressure at the surface, and g is the acceleration due to gravity. Units are in $10^{10}\,\mathrm{kg\,s^{-1}}$. Positive (negative) values of ψ^{mms} correspond to a clockwise (counterclockwise) circulation as in the NH (SH) winter cell. Note that we have not taken the time mean as is commonly done as we wish to apply SSA directly to anomalies w.r.t. the climatological mean of $\psi^{\mathrm{mms}}(\phi, p, t)$. As we are explicitly interested in the South Pacific, the zonal mean is taken over the domain 120°–300°E.

Zonal wind anomalies are explicitly linked to the meridional temperature gradient through the thermal wind equation, here defined as

$$\mathbf{v}_T=\frac{1}{f}\mathbf{k}\times\nabla_p(\Phi_{300\mathrm{hPa}}-\Phi_{700\mathrm{hPa}}), \qquad (2)$$

where f is the Coriolis parameter, $\mathbf{k}$ is the unit vector perpendicular to Earth's surface, ∇_p is the gradient on a constant pressure surface, and Φ is the geopotential at the pressure level indicated by the subscript. Note that this calculation directly invokes both the hydrostatic and geostrophic approximations, with the latter not being applicable in the immediate vicinity of the equator (Dickey et al. 2007), which we mask out of our calculations.

In the sections to follow we undertake a systematic examination of atmospheric variability in the region (90°S–0°, 120°–300°E). We perform an initial EOF/PC analysis of the SH troposphere, appropriately cosine of the latitude weighted, considering covariances of Z_g simultaneously calculated at 300, 500, and 700 hPa. The consideration of covariances from these three levels by construction isolates the equivalent barotropic structures of the troposphere. EOF/PC analysis reduces the dimensionality by progressively partitioning the variance according to invariant patterns. In all calculations we account for the total variance, meaning that the number of PCs is equal to either the number of model grid points or to the number of time steps, whichever is the greater. This necessitates the calculation of typically more than 20 000 EOFs/PCs. SSA is then applied to deconstruct the multiscale EOF/PC modes into their constituent components for given time scales. The SSA-reconstructed components are then analyzed to determine the amount of variance, attributable to either the internal dynamics of the waveguides (jets) or to tropical forcing, relative to the total variance explained by the given EOF/PC mode.

3. Multiscale spectral analysis of the PSA

We first apply EOF/PC analysis to reduce the dimensionality of the data and to verify that the JRA-55 can reproduce the now familiar patterns and variability associated with SAM and the PSA modes. Here, and for convenience, we apply the usual interpretations of the leading EOF patterns of $Z_g^{500\mathrm{hPa}}$ (i.e., that the SAM corresponds to EOF1, and the PSA1 and PSA2 modes are contained within the variability of EOFs 2 and 3,

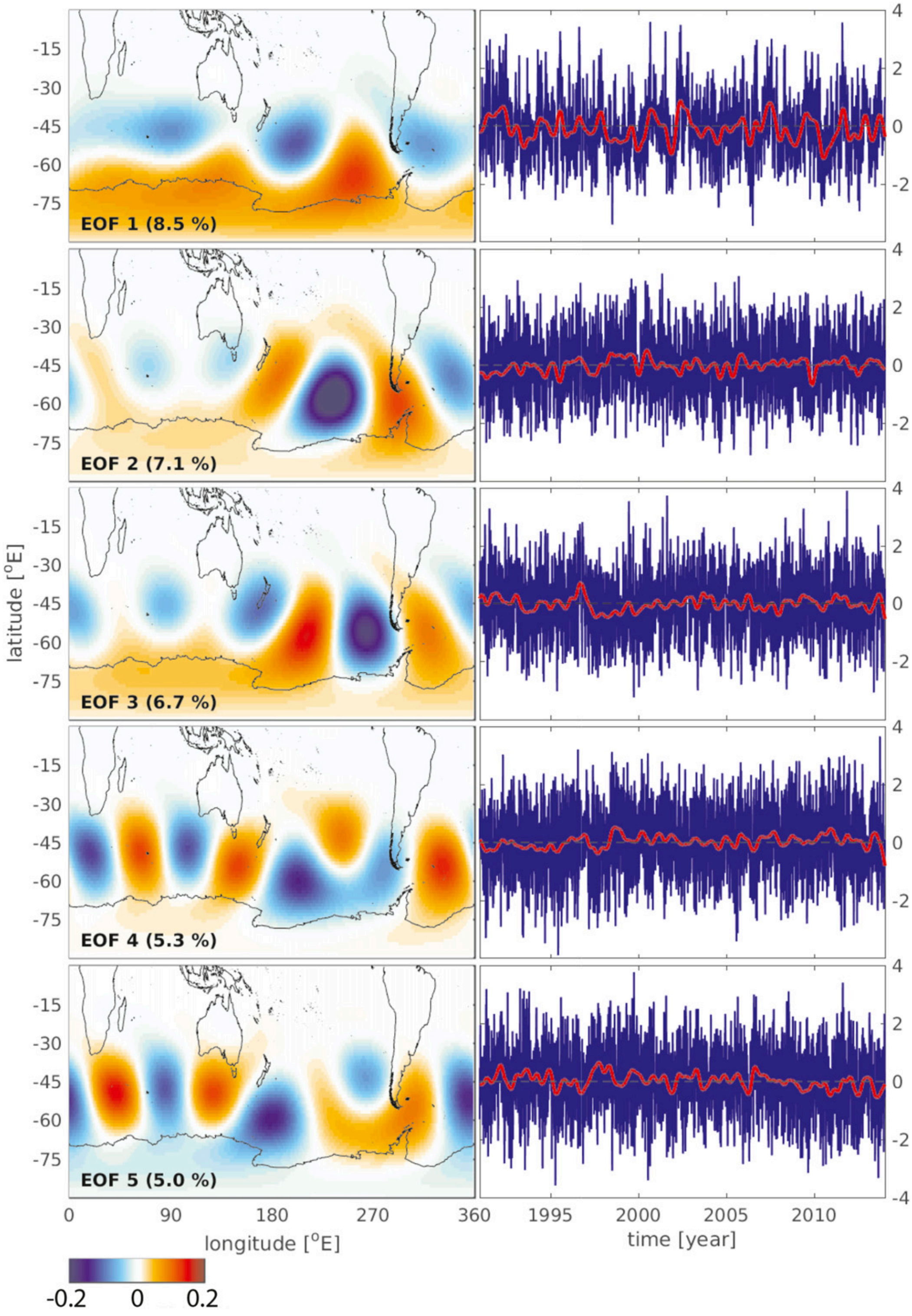

FIG. 2. The leading five EOF patterns and their corresponding PCs calculated from combined 300-, 500-, and 700-hPa Z_g geopotential height anomalies. The variability associated with the low-frequency component is calculated as the 360-day SSA-filtered PC indicated in red is superimposed on the daily PC amplitudes in blue.

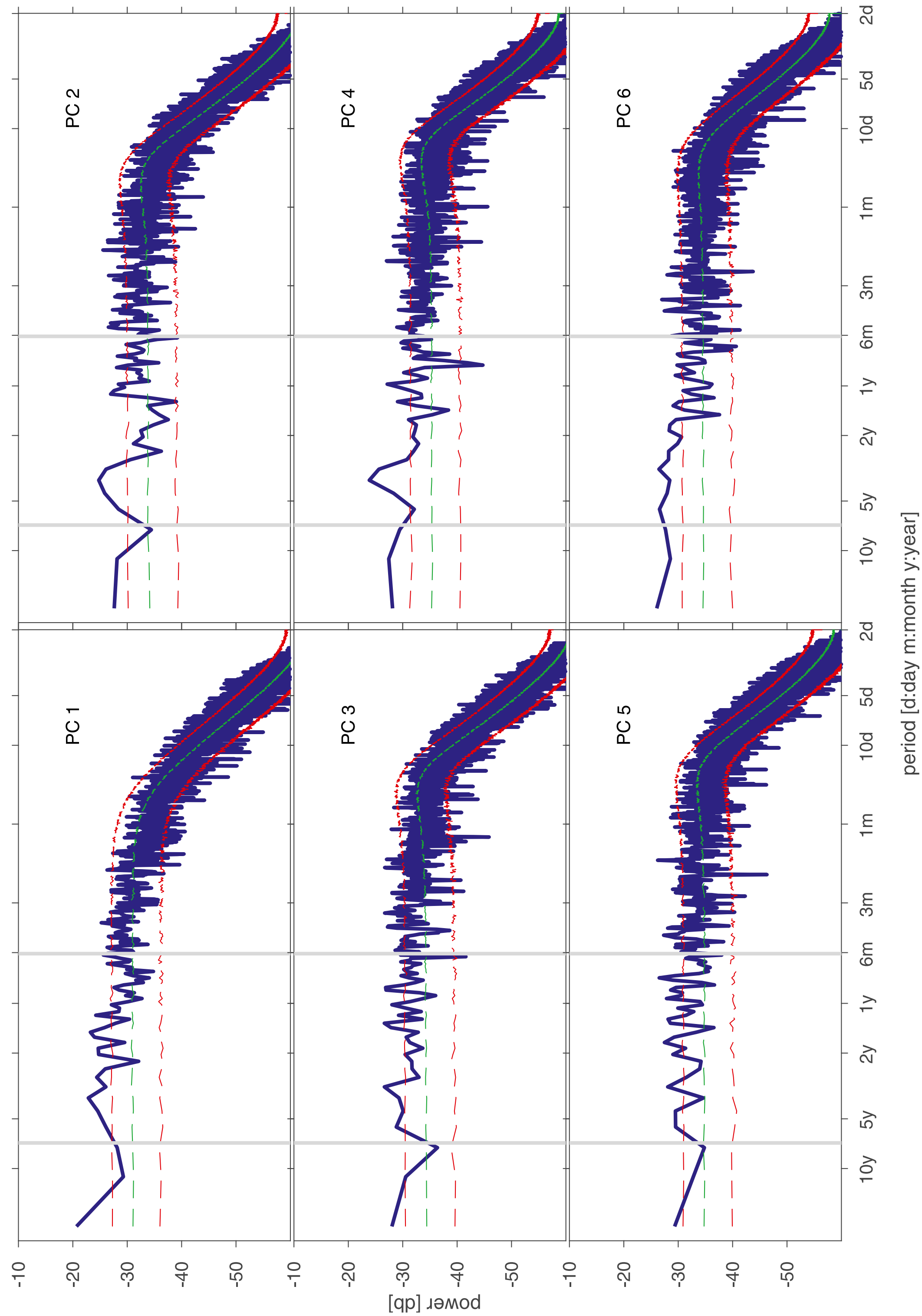

FIG. 3. Log–log plots of power spectra in decibels (db) of an AR(2) process fit to the PCs (blue lines) of the leading six empirical $Z_{500\mathrm{hPa}}$ modes described in Fig. 2. The red dashed lines indicate the 5th–95th percentile confidence interval, and the green dashed line indicates the 50th percentile. The gray vertical lines indicate the 7-yr to 6-month time band.

respectively). That said, EOF patterns are in general not necessarily physical patterns but the invariant structures that maximize the variance of a given three-dimensional time series. In general a combination of EOF/PC modes may be required to capture a physical mode. For example, O'Kane et al. (2013) show that the leading 9 EOF/PC modes of $Z_g^{500\mathrm{hPa}}$ are required to represent the planetary wavenumber-3 mode and blocking. We further recognize that there are varying interpretations as to the physical meaning of EOF/PC modes; for example, due to the presence of a wavenumber-3 imprint Ding et al. (2012) consider EOF1 $Z_g^{500\mathrm{hPa}}$ to be a combination of both the SAM and PSA patterns. Whereas Lau et al. (1994) and Mo and Higgins (1998) interpret the PSA1 and PSA2 modes to be an eastward-propagating wave train, Irving and Simmonds (2016) question whether there is a physical basis for interpreting EOF3 (PSA2). To reiterate, here we apply EOF/PC analysis only to reduce the dimensionality of the data before application of SSA.

The SAM is well represented as the EOF1 mode in Fig. 2. The PSA modes are generally regarded as the low-frequency component of EOFs 2 and 3, here displayed in Fig. 2 in terms of the 360-day SSA-filtered PCs 2 and 3. From the PCs of the leading five modes we can already see that the low-frequency component of the annular mode (EOF1), accounts for a significantly greater percentage of the variability than occurs for the PSA modes (EOFs 2 and 3). To determine statistical significance we calculated the power spectra of an AR(1) and AR(2) process (1000 realizations) fit to the PC time series of the leading six empirical modes. We found that an AR(2) process was required to fit the tail of the spectra, shown in Fig. 3 with the corresponding 5th, 50th, and 95th percentile ranges. This analysis reveals a statistically significant peak in power on the 2–7-yr time scale for PCs 2 and 4. In every case—PCs 1 to 6—the spectra reflect multiscale features. Correlation between $Z_g^{500\mathrm{hPa}}$ and the MEI (Wolter and Timlin 2011) (Fig. 4) reveals ENSO influences on the South Pacific troposphere are largest during the austral spring (SON) whereas the austral summer is the period where ENSO most strongly correlates to $Z_g^{500\mathrm{hPa}}$ variability between ±30° latitude.

Many studies of the PSA modes prefilter the data (low pass), typically removing variability on time scales less than 120–360 days (Mo 2000). Subsequent analysis of the leading invariant EOF patterns and their relevance to physical mechanisms can only be meaningful where those patterns account for a significant fraction of the total variance, not the fraction of the variance retained after the data has been filtered. In the following we are interested to quantify the fraction of total variance described by the various frequency components of the multiscale PCs and to ascertain whether these components

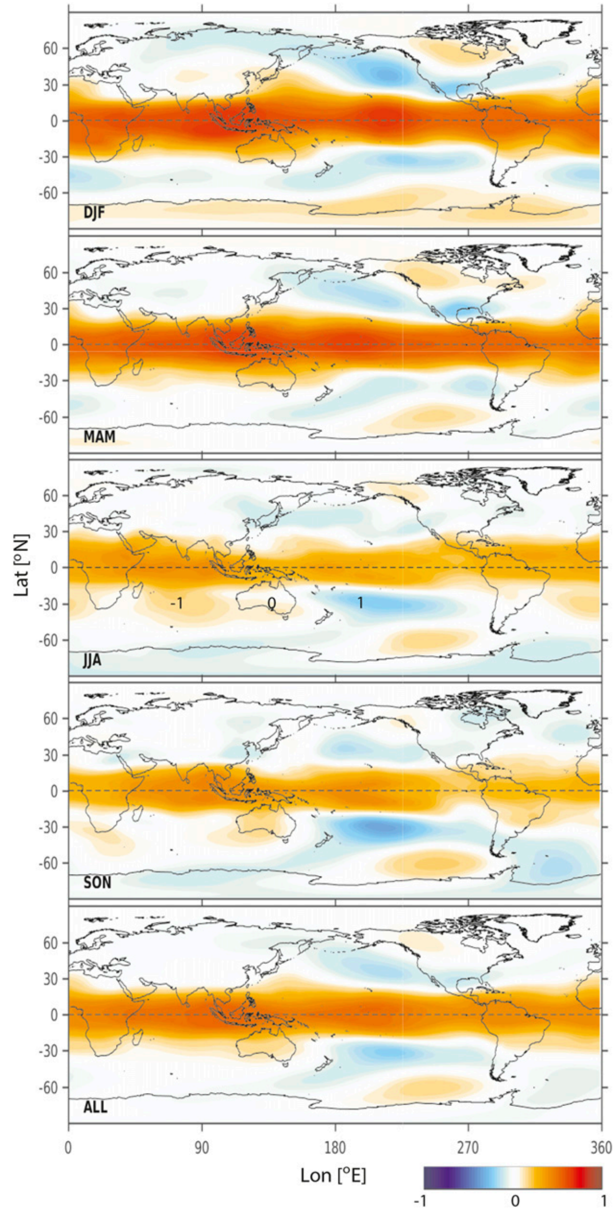

FIG. 4. Correlation of the multivariate ENSO index (MEI) and $Z_g^{500\mathrm{hPa}}$ by season and over the entire period 1958–2013. Only statistically significant correlations are shaded.

[SSA reconstruction component $r_k^M(t)$ (Eq. A2)] arise due to the internal dynamics of the waveguides (subtropical and polar jets) or are manifestations of tropical ENSO dynamics.

a. Geopotential height

To identify any likely ENSO influence on the low-frequency components of the leading EOF/PC modes, we apply SSA to the leading five $Z_g^{500\mathrm{hPa}}$ PCs for an embedding dimension of 360 days (Fig. 5). Here the time

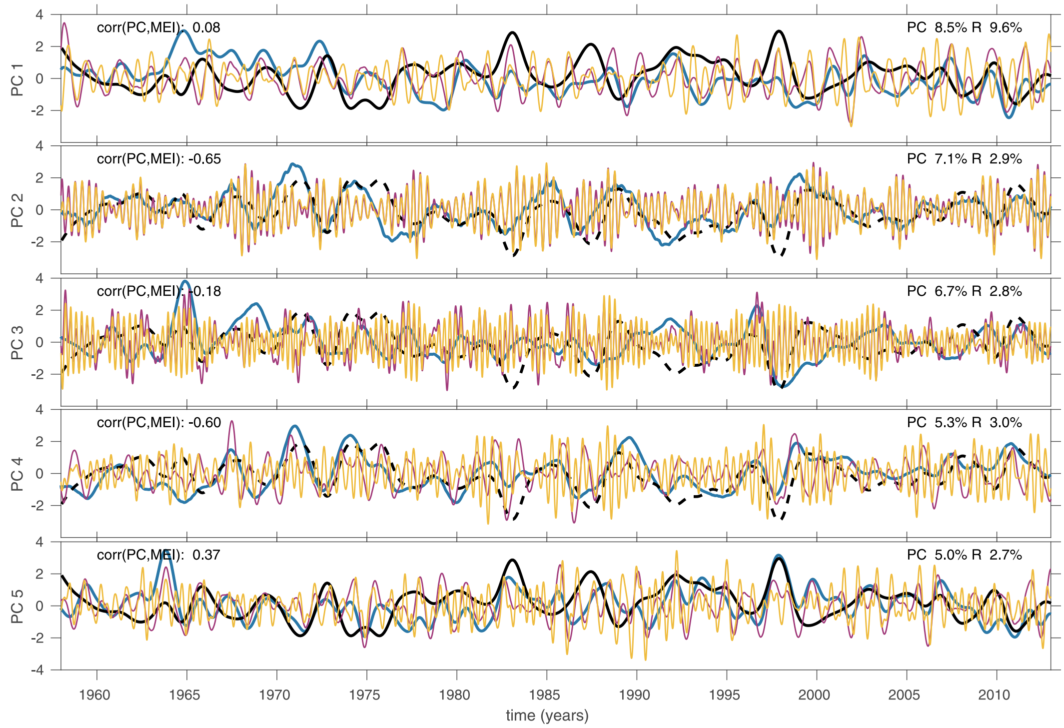

FIG. 5. Time series of the three least oscillating reconstruction components [slowest R_{ns}^M (blue), next slowest (magenta), and fastest (mustard)] of the leading five $Z_g^{500\text{hPa}}$ PCs depicted in Fig. 2 for an embedding dimension of 360 days. ENSO variability is indicated by a similar SSA calculation of the slowest reconstruction component of the MEI for which solid (dashed) black lines are positive (negative) values. The correlation of the least oscillating reconstruction component R_{ns}^M with MEI is indicated in the top left of each panel. The variance explained by the associated EOF/PCA mode and the percentage of the variance of the PC explained by the R_{ns}^M SSA component are shown in the top right of each panel.

series of the three least oscillating SSA reconstruction components [slowest (blue), next slowest (magenta), and third fastest (mustard)] are compared to low-frequency ENSO variability, similarly calculated as the least oscillating SSA reconstruction component $r_{ns}^M(t)$ of the MEI at the 360-day time scale (black). The correlation of $r_{ns}^M(t)$ of $Z_g^{500\text{hPa}}$ with that of the MEI (upper left of each panel in Fig. 5) reveals PCs 2 (PSA1) and 4 to be correlated at the -0.65 and -0.60 levels, respectively. As expected, the leading low-frequency components of the SAM (PC1), PSA2 (PC3), and PC5 are not at all well correlated with ENSO.

Thus far we have confirmed significant correlation of the PSA1 with ENSO and identified PC4 as another higher-order mode influenced by tropical Pacific interannual variability. On synoptic-to-intraseasonal time scales, O'Kane et al. (2016b) identified quasi-stationary regime states in the South Pacific, associated with blocking, with the same patterns as the PSA modes. This raises the question as to whether the PSA should more accurately be characterized, not simply in terms of the low-frequency component of EOF/PCA 2 and 3, but as multiscale regimes manifesting on a hierarchy of time scales? If the answer is yes, then what fraction of the variability arises purely due to dynamics internal to the waveguide relative to that due to tropical influences, and what are the mechanisms by which each occurs? O'Kane et al. (2016b) examined internal waveguide dynamics, blocking, and persistent patterns of the SH troposphere, including Rossby wave sources, velocity potential, wave activity flux, and potential vorticity. On synoptic time scales, they found little evidence of sustained tropical sources, rather that local sources within the waveguide were the primary mechanism for the generation of stationary Rossby waves. We will confine the rest of our analysis to quantifying the role of the tropics on multiscale PSA variability.

We identify the patterns associated with the SSA r_{ns}^M reconstruction component, considering a range of time scales from 2 to 480 days, by correlation with $Z_g^{500\text{hPa}}$ height anomaly time series [Eq. (A6)]. In the austral winter (Fig. 6), the SAM (PC1) pattern is strongly zonal at high latitudes with a wavenumber-3 structure at the midlatitudes. At intraseasonal time scales (10–90 days), the wintertime PC2 (PSA1) and PC3 (PSA2) patterns

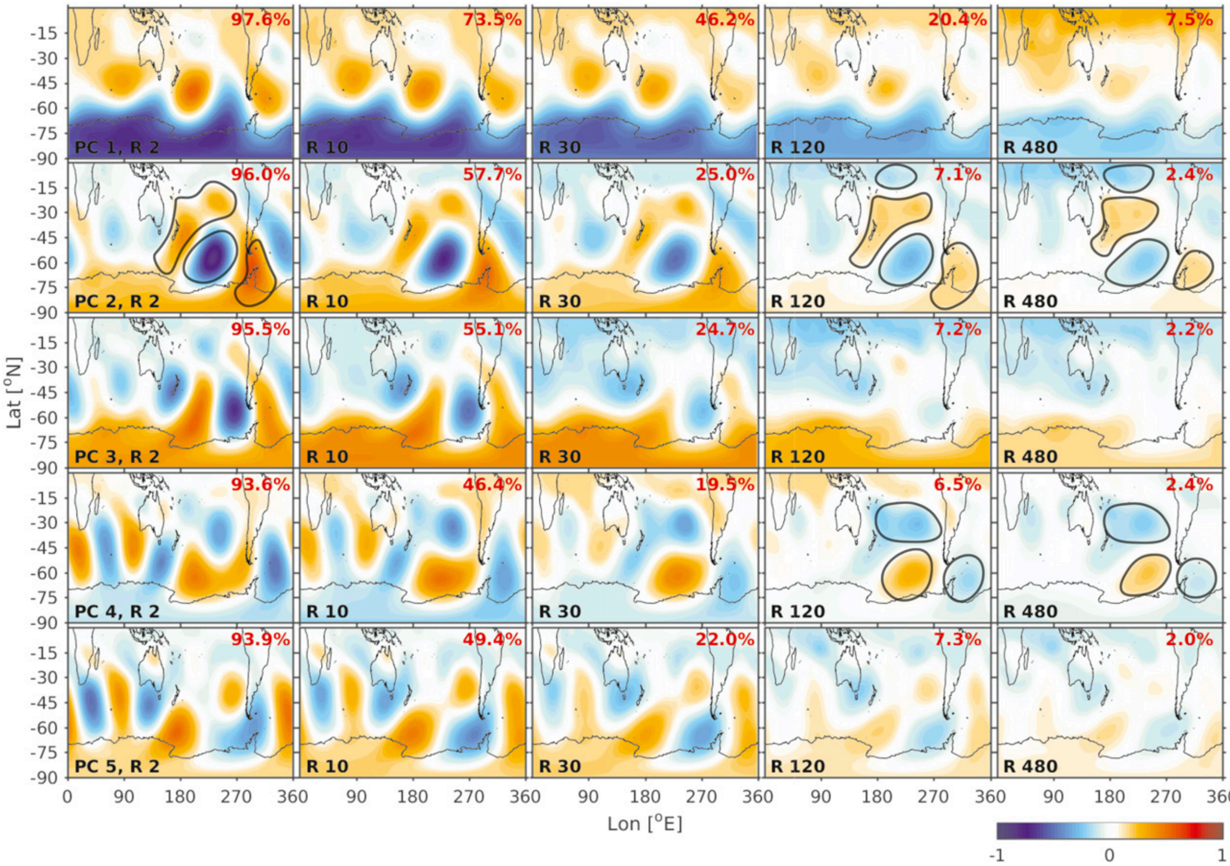

FIG. 6. Winter (JJA) spatial pattern of the least oscillating SSA reconstruction component R_{ns}^{M} of the leading five $Z_g^{500\text{hPa}}$ PCs at embedding dimensions of 2, 10, 30, 120, and 480 days. The pattern of the slowest reconstruction component of a given mode is obtained by correlating with the time series of $Z_g^{500\text{hPa}}$ anomalies. Black outlines indicate structures previously associated with stationary Rossby wave trains. The percentage of the variance of the PC, for a given embedding, explained by the R_{ns}^{M} SSA component is shown in the top right of each panel.

closely resemble those reported by Mo and Higgins (1998). The pattern is largely invariant across time bands, while the explained variance progressively decreases as the embedding dimension increases. The total in-band variance explained by the low-frequency reconstruction component is the difference between the variance at given embedding dimensions as a product of the percentage of variance explained by the PC. Thus, the percentage of the 2–30-day in-band variance (Fig. 6) explained by the least oscillating SSA reconstruction component of the PSA1 (PC2) mode accounts for $\text{R2}(96.0\%) - \text{R30}(25.0\%) = 71.0\%$ of the total variability explained by EOF/PC2. Similarly, the percentage of the variance explained by the least oscillating SSA reconstruction component of the PSA1 (PC2) mode that most highly correlates with ENSO, accounts for only $\text{R120}(7.1\%) - \text{R480}(2.4\%) = 4.7\%$ of the total variability explained by EOF/PC2.

The PSA1 pattern also manifests at all embeddings (from daily to interannual) but weakens as the time scale increases and progressively less of the variance is explained. At the 30-day embedding, the pattern depicting the correlation between PC2 and the least oscillating SSA reconstruction component (R30) (Fig. 6) reflects the tendency for very long-lived persistent blocks to form in the South Pacific. At 120- and 480-days embedding, the PC2 R120 and PC2 R480 patterns highlighted (bold outlines Fig. 6) in the Pacific are composed of a residual PSA1 signal and an emerging ENSO signal in the tropics. This feature is commonly misrepresented as a Rossby wave train (Cai et al. 2011) when there is little evidence of any sustained equatorial Rossby wave source at this time scale. From Fig. 1, we see Rossby wave sources in the SH largely located in the subtropical (JJA) and polar (DJF) jets. The SSA pattern for PC3 reveals the PSA2 mode to be largely expressed at short time scales, an indication that internal waveguide processes are dominant. For PC4, where we find significant correlation with ENSO at time bands greater than 120 days, we largely observe the correlation patterns of $Z_g^{500\text{hPa}}$ with the leading SSA

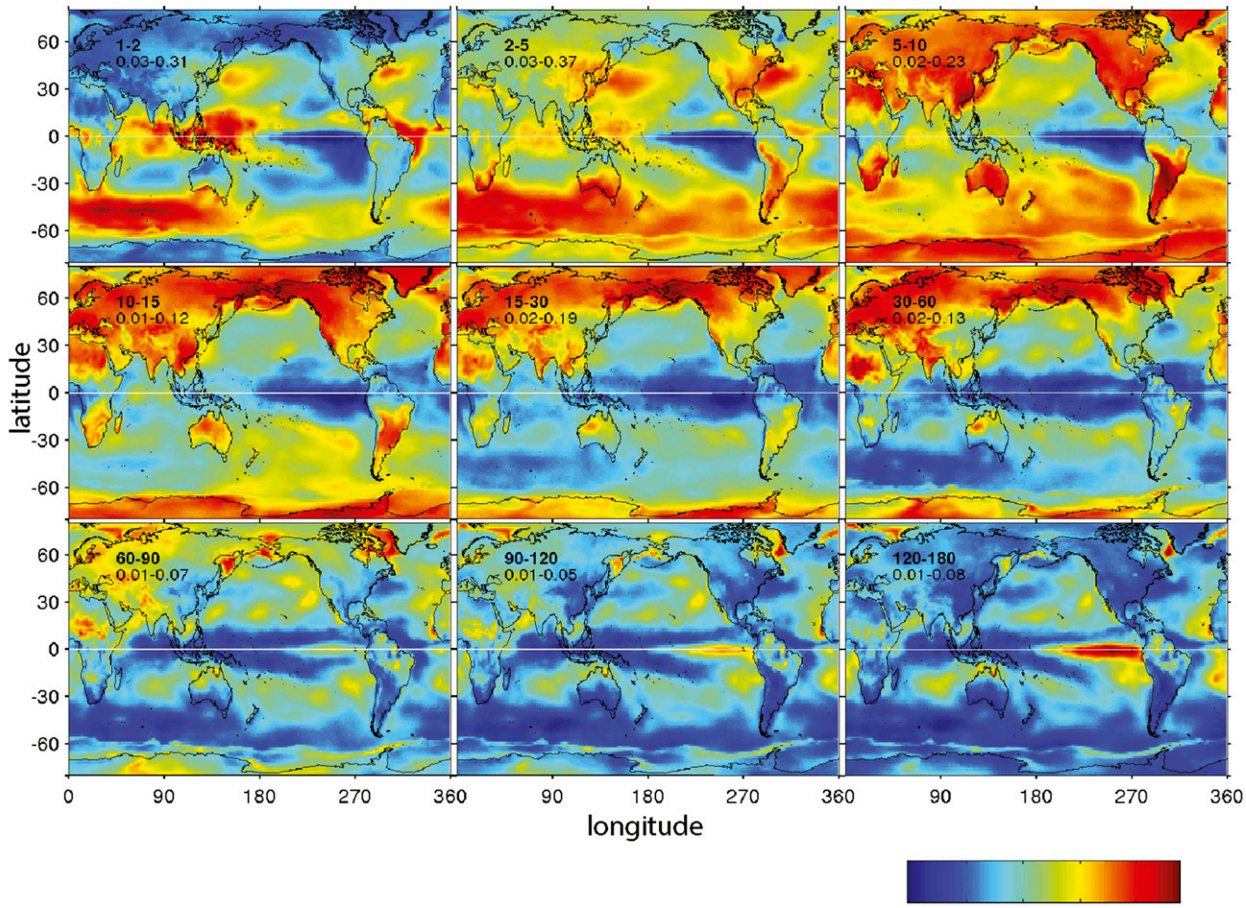

FIG. 7. Fractional in-band variance of surface air temperature (SAT) variability calculated using daily anomalies from the climatological annual mean over the JRA-55 period. Time scale bands (bold font) are in days and relative explained variance range [min–max values (normal font)] as a fraction of the total variance are given in the top left on the Eurasian continent. The shading is given by the color bar at the bottom right with end points determined by the min–max values. Shading is scaled to the variance range in each subplot such that red indicates the maximum relative explained variance and blue indicates the minimum. The combined variance in each band sums to $1 - \lambda_{M=180}$. Embedding dimensions shown correspond to time bands of 1–2, 2–5, 5–10, 10–15, 15–30, 30–60, 60–90, 90–120, and 120–180 days.

reconstruction component to be a residual of the much greater variability observed on time scales shorter than 30 days. In Fig. 6 we highlight the consistent pattern in the PSA1 mode across time scales from daily to interannual. The patterns for the austral summer differ only in that they are less intense and slightly more zonal. Similar structures are found when correlating temperature (not shown), again revealing no significant coherent asymmetries in the variability at the tropics but rather the emergence of an equatorial signal, which is the source of the correlation with ENSO.

b. Temperature

To further examine the source of variance at given time bands, we consider the fractional in-band variance of surface air temperature (SAT), again calculated using daily anomalies from the climatological annual mean over the JRA-55 period 1958–2013. Here we do not apply EOF/PCA prior to SSA and so calculate the fraction of the total variance for given time bands. In Fig. 7, we consider time scale bands of 1–2, 2–5, 5–10, 10–15, 15–30, 30–60, 60–90, 90–120, and 120–180 days. The relative explained variance range is given as a fraction of the total variance in the system, where the shading is determined according to end points given by the minimum/maximum values indicated in each panel. Here red indicates the maximum relative explained variance and blue indicates the minimum. The combined variance in each band sums to $1 - \lambda_{M=180}$. On 1–2 days, the variance is largely located over the Maritime Continent and in the Indian Ocean. This sector of the Indian Ocean troposphere has been shown by O'Kane et al. (2016b) to be a major source of both baroclinic and barotropic instability on short time scales. On 2–5 days, the variability is representative of the SH midlatitude jet, and

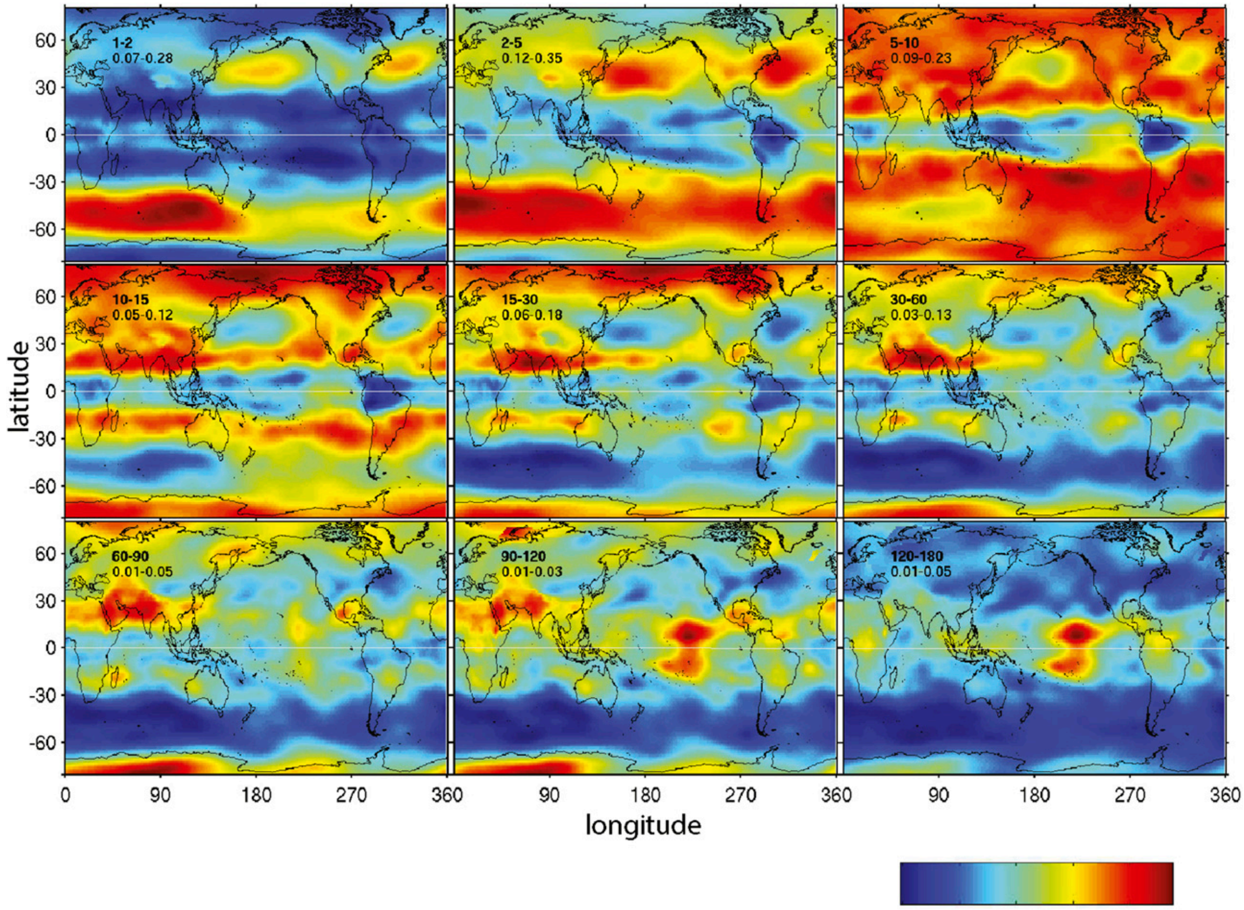

FIG. 8. As in Fig. 7, but for temperature at 500 hPa (i.e., $T^{500\mathrm{hPa}}$).

disturbances downstream of the major topographic features (i.e., the Rocky and Himalayan Mountains in the NH and the Andes in the SH). On 5–10 days, heating due to the landmasses is particularly evident; however, only in the SH is the variance over the oceans large. Variance in the equatorial Pacific starts to emerge beyond 60 days and is clearly characteristic of ENSO beyond 120 days.

At 500 hPa (Fig. 8), the SH fractional in-band variance on 1–2 days, is again largest in the Indian Ocean (SH) and downstream of the Rockies and Himalayas (NH). On 2–5 days, the SH variance spans the midlatitudes, contracting to the subtropical jet at 5–10 days. At 15–90 days, the Maritime Continent has by far the largest variance signal, presumably due to the Walker circulation and the Madden–Julian oscillation. As for SAT, variance in the tropical Pacific is in the 90–120- and 120–180-day time bands, and associated with ENSO.

c. *Thermal wind*

We next consider the role of the thermal wind $\mathbf{v}_T$ in modulating the jets. The leading two EOF/PCs of the meridional component of $\mathbf{v}_T$ project onto the wave-5 structure of the tropospheric circulation (Fig. 9). The dynamics and metastability of this SH circumglobal wave train have been discussed in detail in the recent study of O'Kane et al. (2016b) and we refer the interested reader to that discussion. The low-frequency component (360-day filtered) of the leading two meridional modes are uncorrelated with the MEI and account for a tiny percentage of the explained variance. As suggested by the small amount of variance explained by the two leading meridional modes, the eigenspectrum of the EOF/PCA requires many modes to explain a significant percentage of the variance. The leading zonal PC1 and PC2 modes of $\mathbf{v}_T$ similarly account for a small fraction of the total variance ($\approx$2%); however, a significant percentage of the explained variance of each mode is contained in a slow (tropical) signal. The greatest (least) latitudinal extent over which the correlation of $\mathbf{v}_T$ with the MEI occurs over the Pacific during the austral summer (winter) (Fig. 10).

The role of ENSO in modulating the low-frequency variability of the zonal component of the thermal wind is

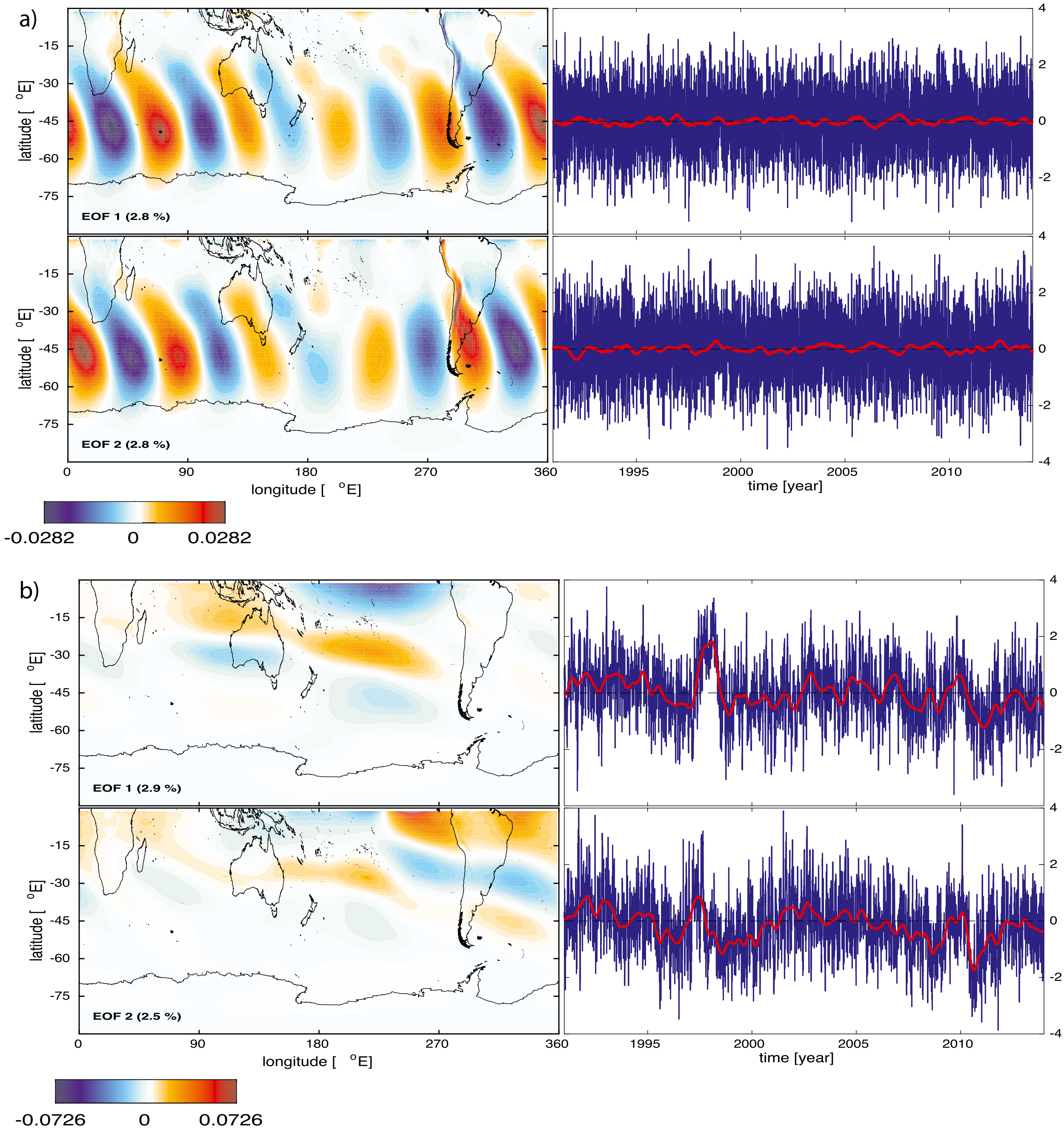

FIG. 9. The leading two EOF patterns and PC time series of the (a) meridional (v) and (b) zonal (u) components of the thermal wind $\mathbf{v}_T$. The variability associated with the low-frequency component is calculated as the 360-day SSA-filtered PCs indicated in red.

confirmed by correlations of 0.936 and 0.559 for the least oscillating SSA reconstruction component of the leading two zonal $\mathbf{v}_T$ PCs at the 360-day time scale (Fig. 11). The higher-order zonal $\mathbf{v}_T$ modes are largely uncorrelated with ENSO. Again we make the point, that the variance explained by the leading two zonal $\mathbf{v}_T$ modes that highly correlates with ENSO, is only a small fraction of the percentage of the total variance at 360 days embedding described by the PC. The AR(2) fit to the power spectra of the leading zonal $\mathbf{v}_T$ PCs 1 and 2 modes show significant power at interannual time scales (Fig. 12). The spatial patterns of the leading SSA reconstruction component r_{ns}^{M} at given embeddings of the zonal $\mathbf{v}_T$ modes, are obtained by correlation with the zonal $\mathbf{v}_T$ anomalies. Rows 1 and 2 of Fig. 13, correspond to the least oscillating SSA reconstruction component r_{ns}^{M} from

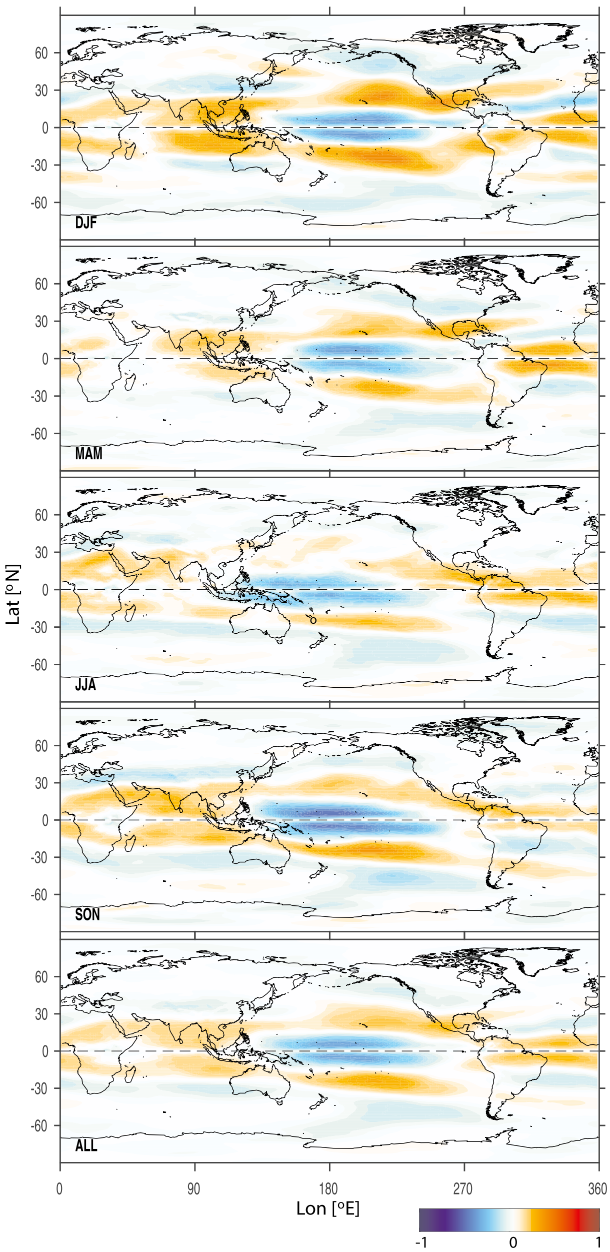

FIG. 10. Correlation of the zonal component of the thermal wind with ENSO (MEI) by season and over the entire period 1958–2013.

PCs 1 and 2. These components are highly correlated with ENSO at embeddings longer than the seasonal time scale, with similar patterns to the associated EOFs (Fig. 9). The in-band variance for the 120–480-day time band corresponds to R120(30.6%) − R480(15.9%) = 14.7% and R120(24.1%) − R480(13.7%) = 10.4% of the total variance explained by PCs 1 and 2, respectively. SSA reconstruction components for PCs 3 and 4 (rows 3 and 4) are not well correlated to the MEI, despite having a zonal wave train structure very similar to the PSA1 and PSA2 geopotential height patterns. That is, the PSA patterns manifest on synoptic scales in PCs 3 and 4 of the thermal wind are independent of tropical forcing. The least oscillating SSA reconstruction components of the higher-order zonal thermal wind PCs have little expression nor variance beyond the 30-day time band, a further indication that internal waveguide processes dominate the higher-order modes of $\mathbf{v}_T$.

d. Hadley circulation

Many studies have focused on the expansion of the Hadley circulation in response to global warming (Hu and Fu 2007; Lu et al. 2007), and in response to El Niño (Oort and Yienger 1996; Lu et al. 2008; Nguyen et al. 2013; Freitas et al. 2016). For example, Lu et al. (2008) found large-amplitude El Niño events could produce a contraction and strengthening of the Hadley circulation. Recent modeling studies by Tandon et al. (2013) and Freitas et al. (2016) found that thermal forcing applied to the equatorial Pacific in a narrow band (between 5°S–5°N) could stimulate an *El Niño–like* Hadley circulation contraction and concomitant poleward shift of the jets. These modeling studies show that small changes to the meridional structure of the thermal forcing have the potential to significantly modulate the circulation response. However, the aforementioned studies largely consider differences between periods or, composites of a few strong El Niño and La Niña events. Here we apply SSA to examine the variability of the Hadley circulation, its correlation to ENSO, and the response of the midlatitude troposphere.

The seasonal climatological ψ^{mms} (Fig. 14) zonally averaged between 120° and 300°E, reveals the structure of the Pacific Hadley circulation. We have chosen this restricted domain to resolve the important regional features of the SH Pacific Hadley circulation, for example, the wintertime subtropical jet (Fig. 14, JJA). Many of these regional Pacific Hadley circulation features are not evident in calculations based on zonal averages over the full hemisphere [see e.g., Fig. 1 of Dima and Wallace (2003)]. As expected, the correlation of ψ^{mms} with the MEI (Fig. 15) over the SH is largest in the austral summer and weakest in the austral winter (JJA). The spring (SON) is the season where the largest significant correlation over the SH midlatitudes (i.e., between 30° and 60°S) occurs. Little significant correlation in the SH midlatitudes is found during the summer. Rather than composite over particular ENSO events (years) (Nguyen et al. 2013), here we directly correlate the ψ^{mms} time series with ENSO. To understand what percentage of Hadley circulation variance occurs in the midlatitudes and its correlation to ENSO, we next conduct an EOF/PCA of ψ^{mms}

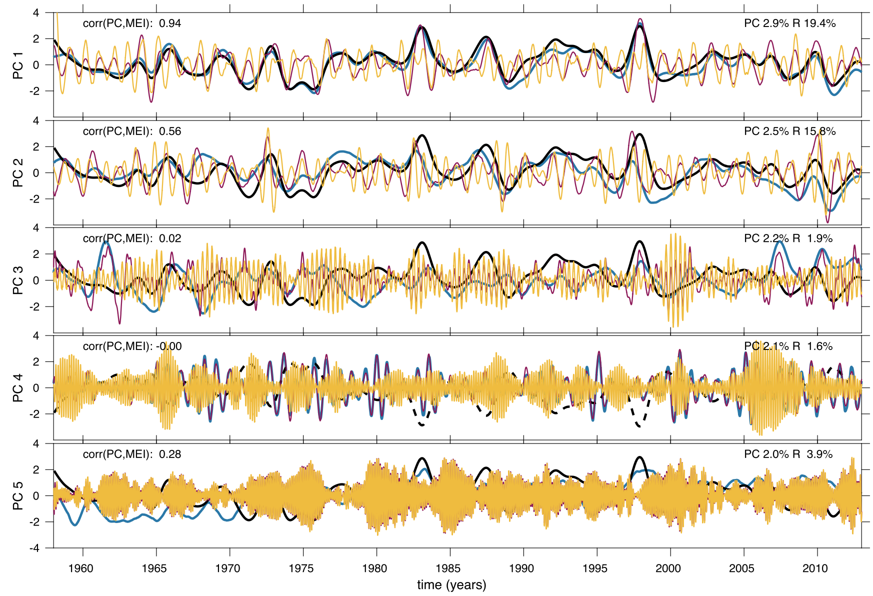

FIG. 11. Time series of the three least oscillating SSA reconstruction components [slowest (blue), next slowest (magenta), and fastest (mustard)] of the leading five PCs of the zonal component of $\mathbf{v}_T$ for an embedding dimension of 360 days. ENSO variability is indicated by the 360-day SSA-filtered MEI [solid (dashed) black lines are positive (negative)]. The correlation of the least oscillating reconstruction component with MEI is indicated in the top left of each panel. Explained variance of the PC and the percentage of the variance of the PC explained by the slowest R_{ns}^{M} SSA component are shown in the top right of each panel.

anomalies w.r.t. the climatological daily mean. The EOF patterns (Fig. 16), reveal most of the variance in both hemispheres occurs at the midlatitudes. The combined variance of EOFs 1 (22.2%), 3 (13.3%), and 6 (6.9%) account for the major Hadley circulation modes of the SH describing 42.4% of the total variance.

On shorter time scales, in-band variances as a fraction of the total ψ^{mms} variance, corresponding to 1–2, 2–5, 5–10, 10–30, 30–60, and 60–90 days are shown in Fig. 17. Consistent with the EOF analysis of the HC (Fig. 16), in Fig. 17, we see large variations at short time scales in the meridional mass streamfunction due to complex interactions of the Ferrel and Hadley cells and due to synoptic-scale dynamical processes internal to the polar and subtropical jets. Here the time band (bold) and maximum/minimum variance is shown in the upper left of each panel, where red (blue) shading indicates maximum (minimum) values with white the zero value. Here we see large signals out to the 30-day embedding, and a positive signal in the tropics during MAM in the 60–90-day band. On the 1–2- and 2–5-day time scales, variance in the South Pacific between 30° and 60°S peaks in the summer and is weakest in the winter. In the 30–60-day window, the most coherent signal occurs about 30°S during the austral summer.

In Fig. 18, we examine the correlation of the least oscillating SSA reconstruction component of the leading six ψ^{mms} modes (PCs) to the time series of ψ^{mms} anomalies, for embedding dimensions 2, 10, 30, 120, and 480 days. Again, only statistically significant correlations are shaded. As expected, the SSA reconstruction components are correlated with ψ^{mms} anomalies in the regions where the ψ^{mms} EOF patterns occur. As the embedding dimension increases the percentage of variance explained by the leading slow SSA reconstruction component decreases, as indicated by the correlation pattern intensities. On the interannual time scale, only a minimal percentage of the total variance is correlated with the ψ^{mms} anomalies.

To ascertain what proportion of the variance is associated with the interannual ENSO signal, we calculate SSA for an embedding dimension of 360 days (Fig. 19). Here we plot the three least oscillating reconstruction components [slowest (blue), next slowest (magenta), and fastest (mustard)] of the leading six ψ^{mms} PCs and calculate the correlation with the 360-day SSA filtered MEI [solid (dashed) black lines are positive (negative)]. We find that the slowest SSA reconstruction component accounts for about 22% of the total variance explained by PC1. Similarly, for the higher-order EOF/PCA

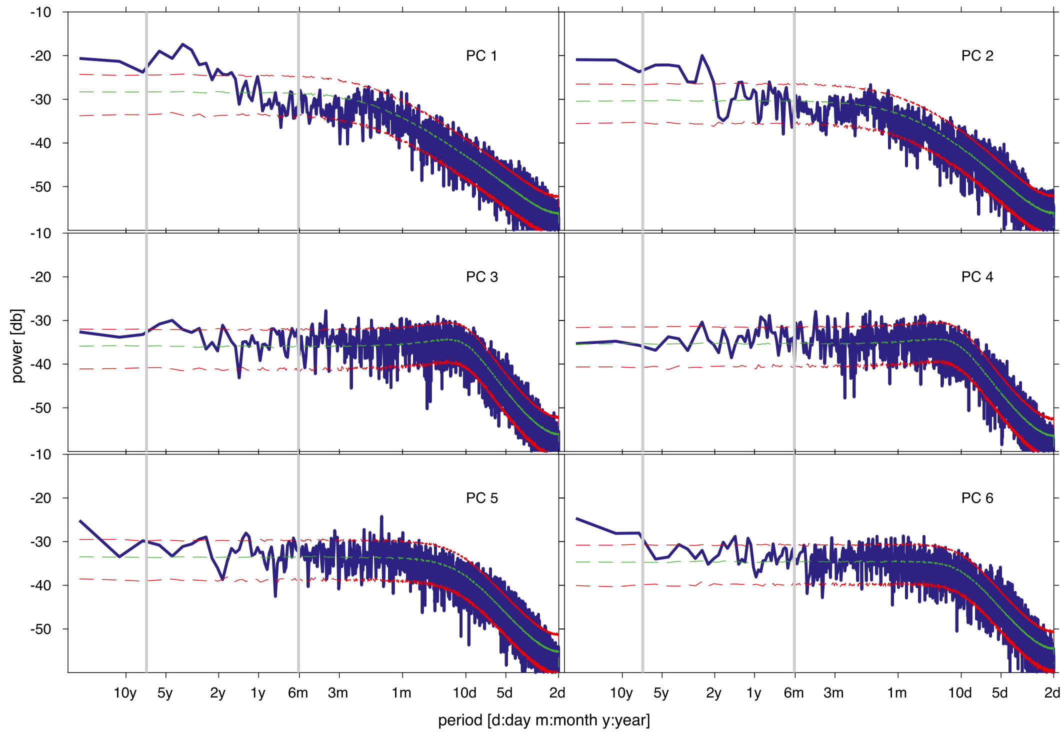

FIG. 12. Power spectra of an AR(2) fit to the leading six PCs of the empirical zonal $\mathbf{v}_T$ modes. The red dashed lines indicate the 5th–95th percentile confidence interval, and the green line indicates the 50th percentile. The gray vertical lines indicate the 7-yr to 6-month time band.

modes, the spectrum of the SSA reconstruction components is relatively flat. None of the modes are well correlated with the 360-day filtered MEI.

e. Discussion

The results described in the previous section highlight the dangers of prefiltering or averaging of data, as forewarned by Lau et al. (1994). Specifically, prefiltering the data via application of a low-pass or running average will remove all variability on time scales shorter than the filtering scale. Subsequent application of EOF/PCA to the low-pass-filtered data means that the retained variance explained by the invariant patterns represents only a fraction of the total variance of the unfiltered data. This is problematic where there is substantive energy at high wavenumbers or where the power in the spectra occurs at short time scales. The general point we make is that the correlation of any low-frequency component of a given EOF/PCA mode with a known physical mode, is only significant when that component accounts for a large percentage of the total variance. We have shown that this is not the case for the slow reconstruction component of PSA1, where the correlation with ENSO resides. We further identified PC4 of $Z_g^{500\mathrm{hPa}}$ as a higher-order mode, whose slow reconstruction component correlates with ENSO at close to the same level as PC2 (PSA1). Further, as PCs 4 and 5 are in quadrature, explain about the same fraction of the total variance, and are separated from the PSA modes and higher-order modes, we argue that they should be considered higher-order analogs of the PSAs 1 and 2 (Fig. 5).

Correlations of the leading SSA reconstruction components with $Z_g^{500\mathrm{hPa}}$ anomalies (Fig. 6), show the PSA patterns (also PCs 4 and 5) to be present and coherent across a large range of temporal scales. At the interannual time scales, the pattern associated with the slow reconstruction component is composed of an emerging tropical ENSO signal and a weak residual PSA pattern. We make the point that correlations are not causal, therefore, interpretations of the patterns derived from regressing time-filtered geopotential height anomalies onto ENSO indices can be erroneously attributed to dynamic processes (e.g., sustained stationary Rossby wave sources). We further note that similar patterns were found for the PSA1 and PC4 and with similarly high (anti) correlations ($\geq$0.6) with ENSO variability.

Further evidence of the role of internal waveguide dynamics in determining the variance on time scales from 1 to 10 days, can be seen in the fractional in-band variances of temperature at the surface and at 500 hPa

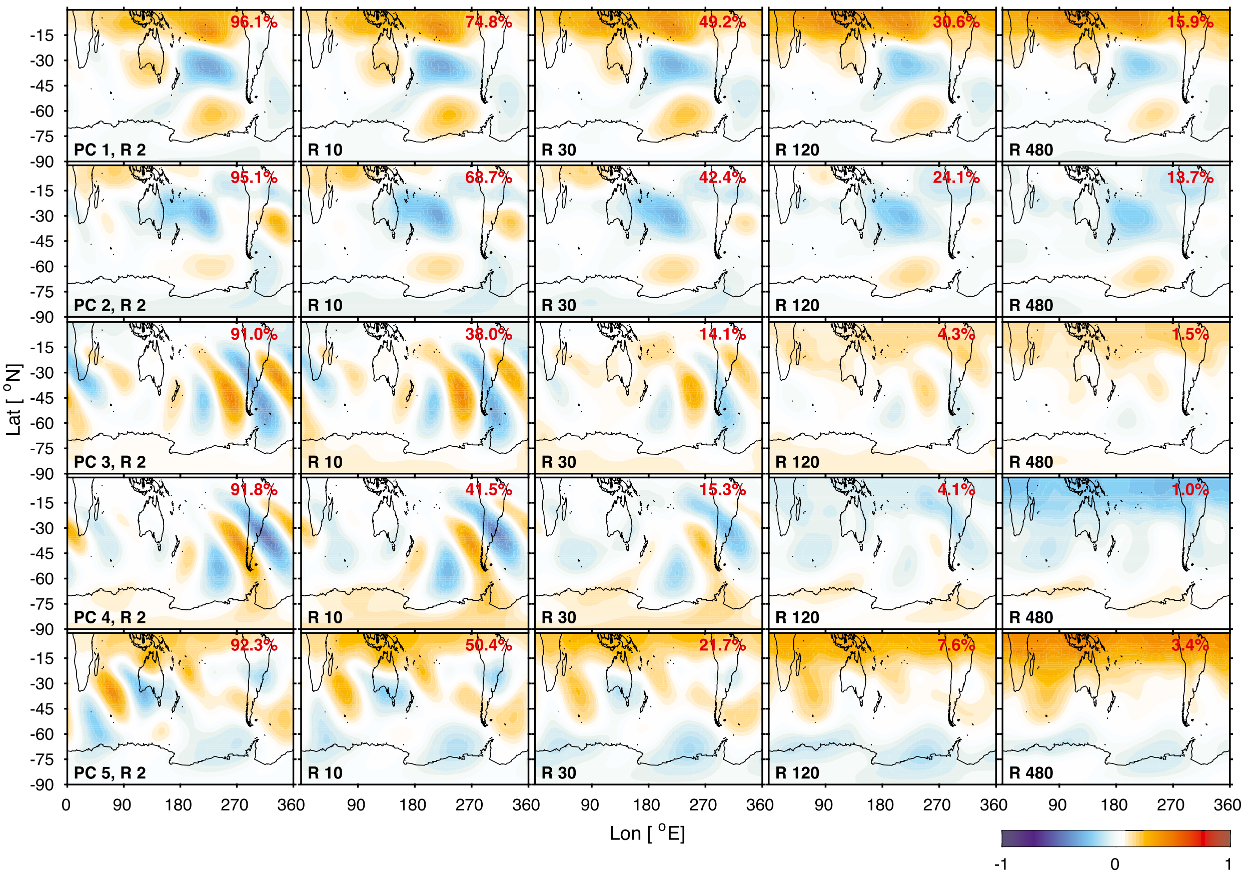

FIG. 13. Annual spatial pattern of the correlation of the least oscillating reconstruction component of the zonal component of the leading five $\mathbf{v}_T$ PCs with $Z_g^{500\text{hPa}}$ anomalies at embedding dimensions of 2, 10, 30, 120, and 480 days. The percentage of the variance of the PC, for a given embedding, explained by the R_{ns}^M SSA component is shown in the top right of each panel.

(Figs. 7 and 8). On time scales between 10 and 60 days at 500 hPa, the subtropics and Indian subcontinent contain the majority of the variance (Fig. 8), presumably associated with the monsoon and MJO. The central and eastern equatorial Pacific is the major source of variance from 91 to 180 days as ENSO variability manifests at the surface (Fig. 7).

The leading modes of the meridional component of $\mathbf{v}_T$ (Fig. 9) were found to comprise a propagating mode that projects onto the SH circumglobal waveguide (O'Kane et al. 2016b). The slow component of these modes represents internal waveguide processes with many modes required to explain a significant proportion of the total variance. The slow SSA reconstruction components (Fig. 11), were found to explain between 20% (PC1) and 15% (PC2) of the variance of the leading two zonal $\mathbf{v}_T$ modes, and were highly correlated with ENSO. However, these slow reconstruction components accounted for only a fraction of the total variance. As mentioned earlier, the zonal $\mathbf{v}_T$ shows a very significant proportion of the variance to be contained at the fast scales. Correlation maps of the slow SSA reconstruction component and the zonal thermal wind modes (Fig. 13) largely resemble the leading two EOF modes. For the PC1 SSA slow reconstruction component, the equatorial signal strengthens with increasing time, whereas the dipolar pattern poleward of 15°S weakens. The slow reconstruction components of PCs 3 and 4 reveal a wave train in the South Pacific on time scales out to 30 days. These PSA-like patterns are associated with blocking in the region to the east of New Zealand (Renwick and Revell 1999; Renwick 2005; O'Kane et al. 2016b). Overall our spectral analysis points to the modulation of the jet by the thermal wind as the origin of interannual ENSO variability in the midlatitudes.

Another potential source of tropical variability in the midlatitude troposphere is the Hadley circulation. We considered Pacific ψ^{mms} variability in order to account for the seasonal splitting of the jet (Fig. 14). We found the largest amplitudes in seasonal maps of the correlation of ENSO and the mean ψ^{mms} Hadley circulation (Fig. 15) to be in the tropics during the austral summer,

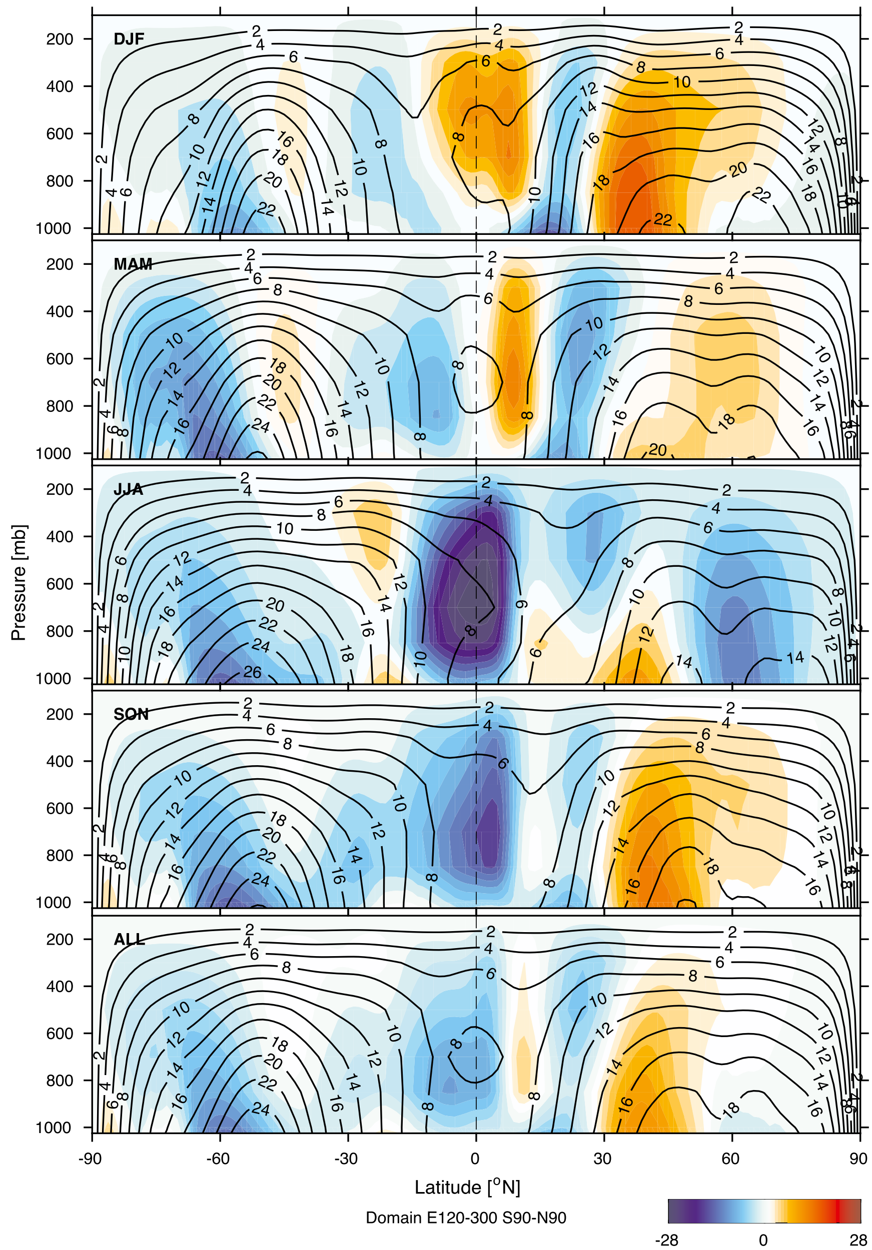

FIG. 14. The seasonal time mean (shaded) meridional streamfunction $\psi^{\mathrm{mms}}(\phi, p)$ zonally averaged over the domain 120°–300°E with variability (contours) overlaid. ALL corresponds to the mean over the entire period 1958–2013; $\psi^{\mathrm{mms}}(\phi, p)$ is in units of $10^{10}\,\mathrm{kg\,s^{-1}}$, and contour intervals are in units of $10^{10}\,\mathrm{kg\,s^{-1}}$.

and at the SH midlatitudes in the austral spring. However, for unfiltered data, an EOF/PCA of anomalous ψ^{mms} (Fig. 16) showed the majority of the variability to reside in the midlatitudes poleward of 30°. Fractional in-band variances (Fig. 17) further supported the idea that the largest fraction of the total ψ^{mms} variability occurs on short time scales in the midlatitudes whereas, on interannual time scales (Fig. 18), the slow midlatitude ψ^{mms} SSA reconstruction components (Fig. 19) are largely unconnected to ENSO.

In this study we have focused on the mechanisms by which the low-frequency ENSO variability is communicated to the SH extratropical Pacific and in particular the role of stationary Rossby waves, the HC, and the thermal wind. A more general question concerns the role of stochastic forcing due to fast tropical convection as a cause

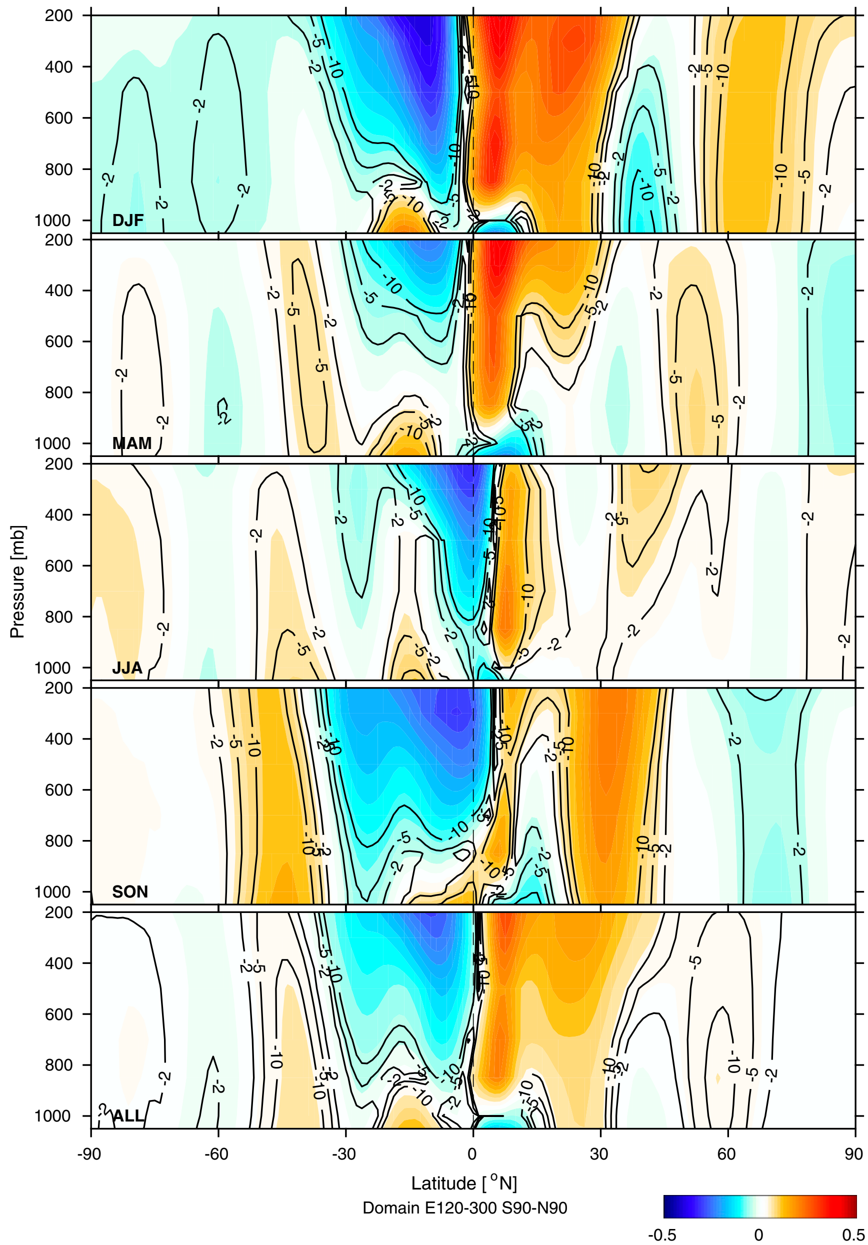

FIG. 15. Correlation of $\psi^{mms}(\phi, p)$ zonally averaged over the domain 120°–300°E with the MEI by season. Only statistically significant correlations are shaded. Contours correspond to the p-value exponent.

of extratropical variability on slower time scales. Franzke (2009) applied empirical mode decomposition, in many respects comparable to SSA, to examine the relative fraction of interannual and longer time scale variability to climate noise of the SAM, NAO, and North Pacific climate teleconnection indices. While our results indicate that a very large fraction of PSA variability manifests on intraseasonal time scales, it remains unclear what fraction of the low-frequency variability of the PSA manifests in part due to fast stochastic physical processes. This is a question we will examine in a future study.

4. Conclusions

In the climate community, the PSA modes have traditionally been defined as the low-frequency variability of EOF/PCA modes 2 and 3 of the SH midtropospheric circulation (Mo 2000), manifesting largely

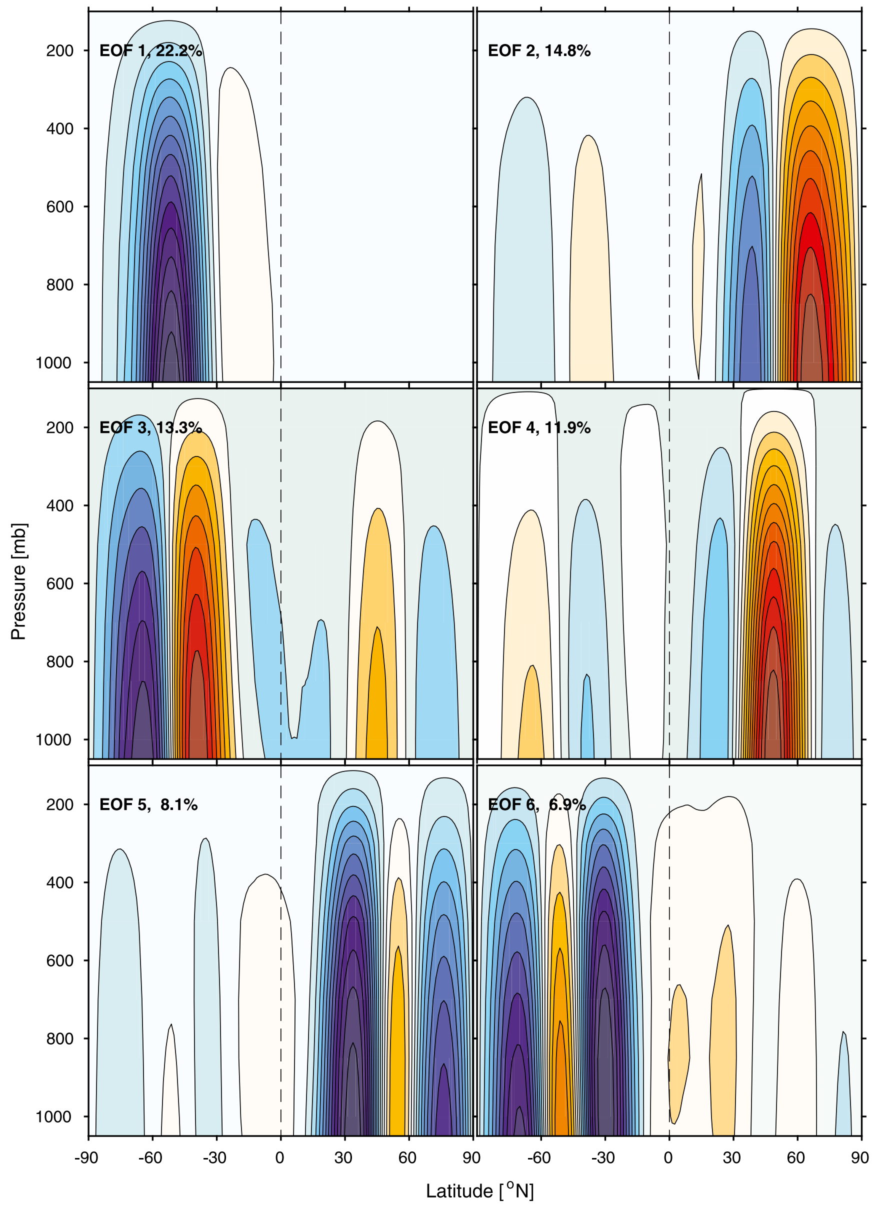

FIG. 16. The leading six EOFs calculated from ψ^{mms} anomalies. Percentage of the total variance explained by each EOF pattern is indicated in the top left of each panel.

in response to the influence of ENSO communicated via stationary Rossby waves (Karoly 1989; Cai et al. 2011). However, because of the presence of reflecting and breaking barriers in all seasons, apart from the austral summer, the perceived role of stationary Rossby waves in determining the PSA modes is in fact inconsistent with the ray tracing theory (Ambrizzi et al. 1995; Li et al. 2015). Calculation of Rossby wave source shows the subtropical and polar jets to be the major source regions for the generation of stationary Rossby waves, with little evidence for sustained equatorial tropical sources influencing the South Pacific. Rather, we see that the source of the low-frequency ENSO signal on the PSA modes arises due to meridional temperature gradients and modulation of the SH midlatitude jets by the thermal winds. These results are consistent with dynamical mode theory (Frederiksen and Frederiksen 1993), the early SSA study of Lau et al. (1994), and the more recent cluster analysis of O'Kane et al. (2016b) that the PSA modes arise largely as intraseasonal oscillations associated with eastward-propagating wave trains and resonant interactions with local disturbances, independent of tropical forcing.

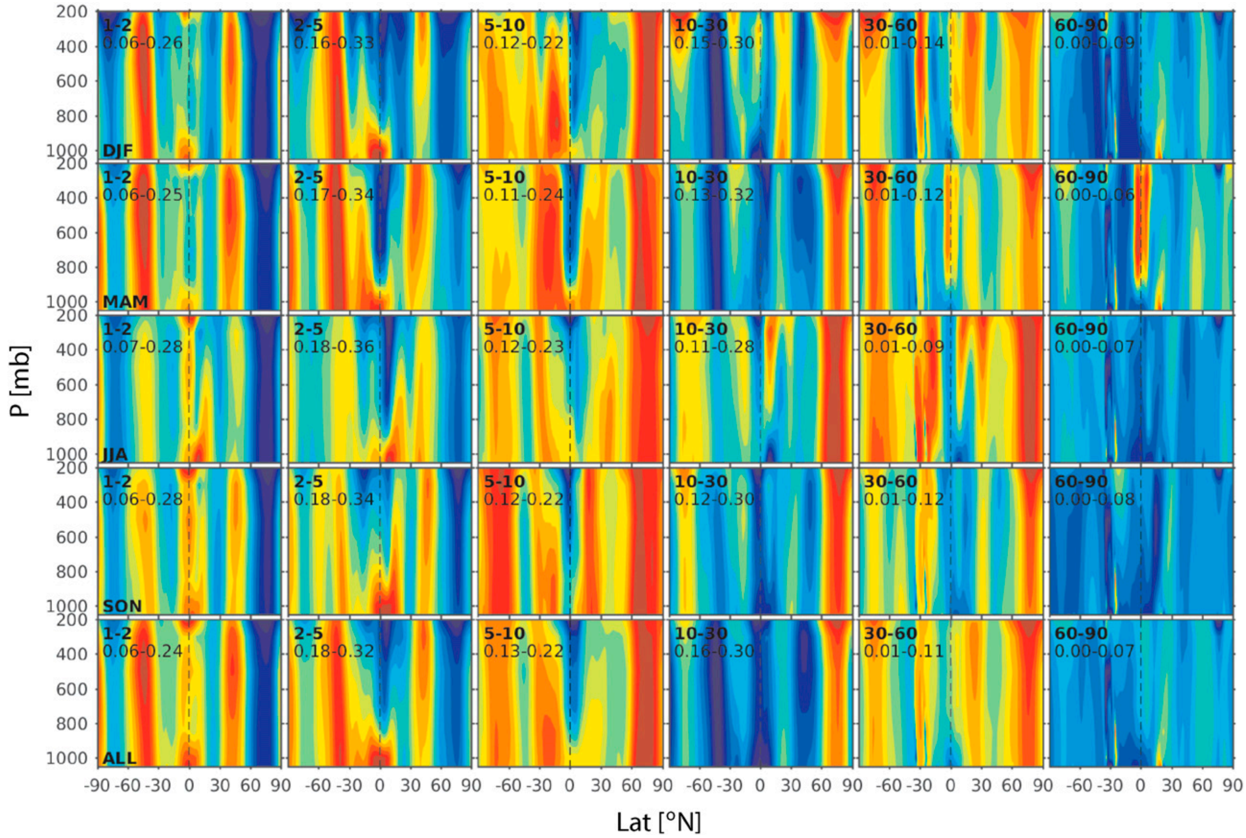

FIG. 17. Fractional in-band variance of ψ^{mms} variability calculated using daily anomalies from the climatological annual mean over the JRA-55. Time scale bands (bold font) are in days and relative explained variance range [min–max values (normal font)] as a fraction of the total variance are given in the top left of each panel. Shading is scaled to the variance range in each subplot such that red indicates the maximum relative explained variance and blue the minimum. The combined variance in each band sums to $1 - \lambda_{M=90}$. Embedding dimensions shown correspond to time bands of 1–2, 2–5, 5–10, 10–30, 30–60, and 60–90 days. Color bar is as in Fig. 7.

Analysis of higher-order modes (PCs 4 and 5), explaining a significant fraction of the total variance (5.3% and 5.0%, respectively), reveal similar characteristics to the PSA modes. Both are indicative of an eastward-propagating wave train where a similarly strong correlation occurs between ENSO and the low-frequency component of the leading mode (PC4), as is found for the PSA1 mode.

Whereas the mean South Pacific Hadley circulation is most highly correlated with ENSO during the summer and spring, most of the variability, as determined by spectral analysis of the airmass transport across meridians, occurs in the midlatitudes within the polar and subtropical jets. EOF/PCA of Hadley circulation variability shows that the correlation of the slowly varying component of the Hadley circulation modes with ENSO is very low, and that the fraction of the total variance described by these modes is small. The patterns associated with the PSA modes were found to manifest at all time scales with the largest fraction of total variance occurring on synoptic time scales. These results, on short time scales, agree with the prior study of blocking in the South Pacific by O'Kane et al. (2016b).

To summarize we find that the PSA is a multiscale nonlinear dynamical mode manifesting on time scales from synoptic to interannual. The major percentage of PSA variability occurs on time scales from synoptic to intraseasonal, is largely independent of persistent coherent tropical processes, and manifests via internal waveguide instabilities and dynamics. The small fraction of the total variability with a tropical signal arises entirely due to modulation of the SH midlatitude jets, via the zonal component of the thermal wind. Finally, we identify a higher-order mode, in terms of the slow components of PCs 4 and 5 of tropospheric geopotential height, with similar characteristics to the PSA, most notably a high correlation of the leading mode (PC4) with ENSO, again arising largely due to the influence of the zonal component of the thermal wind. This observational study provides a basis for a unified theory for

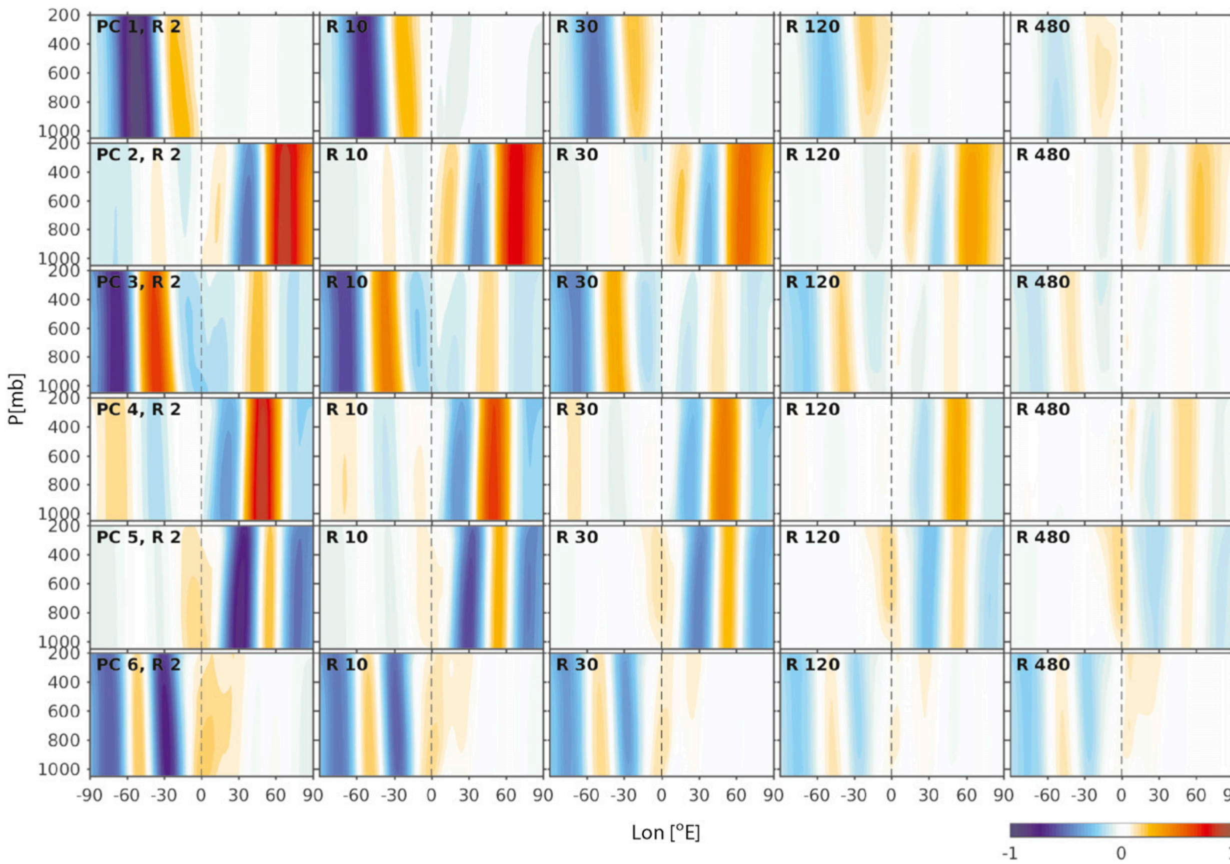

FIG. 18. Correlation of the least oscillating SSA reconstruction component for the leading six ψ^{mms} modes (PCs) with the time series of ψ^{mms} anomalies for embedding dimensions 2, 10, 30, 120, and 480 days. Only statistically significant correlations are shaded.

persistent patterns in the South Pacific that is able to reconcile apparent inconsistencies between earlier ray tracing, dynamical mode, and observational studies.

Acknowledgments. TJO acknowledges funding support of an Australian Research Council Future Fellow (Grant FT120100008). DPM was supported by the Australian Climate Change Science Program. JSR was supported by the Grains Research Development Corporation.

APPENDIX

Singular Spectral Analysis

The general method [Eqs. (A1)–(A4)] described below is the same as employed in Monselesan et al. (2015), and the following paragraph of text is derived from there with only minor modifications. We include it here for completeness.

For all anomaly time series, the variance in selected time bands is computed at each grid point. Nonparametric and data-adaptive singular spectral analysis (SSA) (Elsner and Tsonis 1996; Ghil et al. 2002; Golyandina and Zhigljavsky 2013) is applied to derive the in-band variance following the approach of Monselesan et al. (2015). The method decomposes a time series $\mathbf{x}(t)$ of length L as the sum of reconstructed components derived from covariances $\mathbf{C}(\mathbf{x}, M)$ constructed from lagged versions $\mathbf{x}(t+j-1)$ of $\mathbf{x}(t)$ with $j = 1, \ldots, M \le (L/2)$ up to some maximum lag M, which we refer to as the embedding dimension. The sum of all M eigenvalues λ_k of $\mathbf{C}(\mathbf{x}, M)$ with $k = 1, \ldots, M$ equals the total variance of $\mathbf{x}(t)$. The original time series is recovered as the sum of reconstructed components:

$$\mathbf{x}(t) = \sum_{k=1}^{M} r_k(t), \quad t = 1, \ldots, L, \tag{A1}$$

with

$$r_k(t) = \frac{1}{M} \sum_{j=1}^{M} A_k(t+j-1)\mathbf{e}_k(j), \tag{A2}$$

where $A_k(t)$ are the reconstructed components

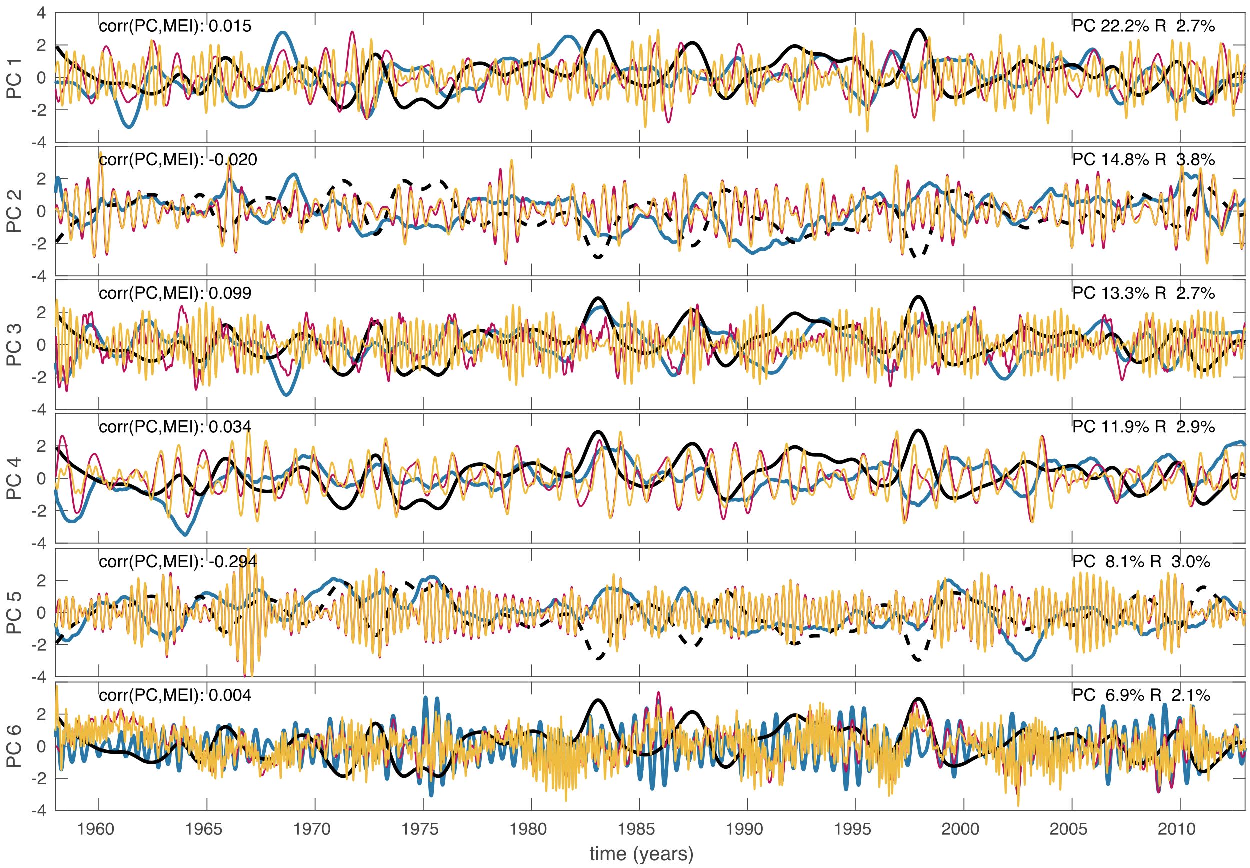

FIG. 19. Time series of the three least oscillating SSA modes [slowest (blue), next slowest (magenta), and fastest (mustard)] of the leading six ψ^{mms} PCs for an embedding dimension of 360 days. ENSO variability is indicated by the 360-day SSA filtered MEI [solid (dashed) black lines are positive (negative)]. The correlation of the least oscillating reconstruction component with MEI is indicated in the top left of each panel.

$$A_k(t) = \sum_{i=1}^{M} \mathbf{x}(t+i-1)\mathbf{e}_k(i) \tag{A3}$$

and $\mathbf{e}_k$ are the eigenvectors of $\mathbf{C}(\mathbf{x}, M)$ such that

$$\mathbf{C}(\mathbf{x}, M)\mathbf{e}_k = \lambda_k \mathbf{e}_k, \quad k = 1, \ldots, M. \tag{A4}$$

The variance explained λ_M by the reconstructed components $r_M(t)$ is computed for the following embedding dimensions M = 2, 5, 10, 15, 30, 60, 90, 120, 180, 240, 360, 480, and 720 in days. In-band variances are then approximated by the variance differences $\lambda_{M_i} - \lambda_{M_{i+n}}$ at each location. The time bands considered here span 1–2, 2–5, 5–10, 10–15, 15–30, 30–60, 60–90, 90–120, 120–180, 180–240, 240–360, 360–480, and 480–720 days.

It is key to recognize that SSA works on the temporal dimension alone, with the spatial maps determined by the dynamic processes in the regions of high temporal variance within a given band. We further apply SSA to time filter the multiscale principal components from the various JRA-55 fields examined. The SSA filtering of the time coefficients of the principal modes for given embedding dimensions, reveal quasi-periodic cycles but also nonperiodic and chaotic behavior. The spatial patterns of the various reconstruction components, for given principal components (modes) at a given embedding dimension (time window), are then simply calculated as the correlation (dot product) between a given SSA reconstruction component and the original anomaly time series. The dominant long-term SSA signals are determined as the least oscillating component relative to switching about zero. For example, considering the variability of the leading principal component of $Z_g^{500\text{hPa}}$

$$\text{PCA}(1) = \sum_{n=1}^{M} r_n^M, \tag{A5}$$

where the least oscillating, SSA mode is selected where $|\sum_{n=1}^{M}\mathbf{e}_k(n)|/\sum_{n=1}^{M}|\mathbf{e}_k(n)|$ has its maximum and where $k = 1, \ldots, M$. A phase preserving filter has also been applied to the retained reconstructed component r_n^M.

Here we have employed the algorithm of Grinsted (www.glaciology.net/software/ssatrend-m). We then calculate the invariant pattern I associated with the least oscillating SSA mode ns, as the correlation between the SSA mode and the full anomaly time series at each location:

$$I(\mathbf{x}) = r_{ns}^{M}(t) \cdot \hat{Z}_{g}^{500\mathrm{hPa}}(\mathbf{x}, t), \qquad (A6)$$

which is subsequently normalized and where the dot $(\cdot)$ is the dot product.

REFERENCES

Ambrizzi, T., and B. J. Hoskins, 1997: Stationary Rossby wave propagation in a baroclinic atmosphere. *Quart. J. Roy. Meteor. Soc.*, **123**, 919–928, doi:10.1002/qj.49712354007.

——, ——, and H. H. Hsu, 1995: Rossby wave propagation and teleconnection patterns in the austral winter. *J. Atmos. Sci.*, **52**, 3661–3672, doi:10.1175/1520-0469(1995)052<3661:RWPATP>2.0.CO;2.

Branstator, G., 1983: Horizontal energy propagation in a barotropic atmosphere with meridional and zonal structure. *J. Atmos. Sci.*, **40**, 1689–1708, doi:10.1175/1520-0469(1983)040<1689:HEPIAB>2.0.CO;2.

Cai, W., P. van Rensch, T. Cowen, and H. H. Hendon, 2011: Teleconnection pathways of ENSO and the IOD and the mechanisms for impacts on Australian rainfall. *J. Climate*, **24**, 3910–3293, doi:10.1175/2011JCLI4129.1.

Clem, K. R., and R. L. Fogt, 2015: South Pacific circulation changes and their connection to the tropics and regional Antarctic warming in austral spring, 1979–2012. *J. Geophys. Res. Atmos.*, **120**, 2773–2792, doi:10.1002/2014JD022940.

Dickey, J. O., S. L. Marcus, and R. Hide, 1992: Global propagation of interannual fluctuations in atmospheric angular momentum. *Nature*, **357**, 484–488, doi:10.1038/357484a0.

——, ——, and T. M. Chin, 2007: Thermal wind forcing and atmospheric angular momentum: Origin of the Earth's delayed response to ENSO. *Geophys. Res. Lett.*, **34**, L17803, doi:10.1029/2007GL030846.

Dima, I. M., and J. M. Wallace, 2003: On the seasonality of the Hadley cell. *J. Atmos. Sci.*, **60**, 1522–1527, doi:10.1175/1520-0469(2003)060<1522:OTSOTH>2.0.CO;2.

Ding, Q., and E. J. Steig, 2013: Temperature change on the Antarctic Peninsula linked to the tropical Pacific. *J. Climate*, **26**, 7570–7585, doi:10.1175/JCLI-D-12-00729.1.

——, ——, D. S. Battisti, and M. Kuttel, 2011: Winter warming in West Antarctica caused by central tropical Pacific warming. *Nat. Geosci.*, **4**, 398–403, doi:10.1038/ngeo1129.

——, ——, ——, and J. M. Wallace, 2012: Influence of the tropics on the southern annular mode. *J. Climate*, **25**, 6330–6348, doi:10.1175/JCLI-D-11-00523.1.

Elsner, J. B., and A. A. Tsonis, 1996: *Singular Spectrum Analysis: A New Tool in Time Series Analysis*. Springer, 164 pp., doi:10.1007/978-1-4757-2514-8.

Franzke, C., 2009: Multi-scale analysis of teleconnection indices: Climate noise and nonlinear trend analysis. *Nonlinear Processes Geophys.*, **16**, 65–76, doi:10.5194/npg-16-65-2009.

Frederiksen, J. S., and C. S. Frederiksen, 1993: Southern Hemisphere storm tracks, blocking, and low-frequency anomalies in a primitive equation model. *J. Atmos. Sci.*, **50**, 3148–3163, doi:10.1175/1520-0469(1993)050<3148:SHSTBA>2.0.CO;2.

——, and H. Lin, 2013: Tropical–extratropical interactions of intraseasonal oscillations. *J. Atmos. Sci.*, **70**, 3180–3197, doi:10.1175/JAS-D-12-0302.1.

Freitas, A. C. V., and T. Ambrizzi, 2012: Changes in the austral winter Hadley circulation and the impact on stationary Rossby waves propagation. *Adv. Meteor.*, **2012**, 980816, doi:10.1155/2012/980816.

——, J. S. Frederiksen, T. J. O'Kane, and T. Ambrizzi, 2016: Simulated austral winter response of the Hadley circulation and stationary Rossby wave propagation to a warming climate. *Climate Dyn.*, doi:10.1007/s00382-016-3356-4, in press.

Ghil, M., and K. C. Mo, 1991: Intraseasonal oscillations in the global atmosphere. Part II: Southern Hemisphere and tropics. *J. Atmos. Sci.*, **48**, 780–790, doi:10.1175/1520-0469(1991)048<0780:IOITGA>2.0.CO;2.

——, and Coauthors, 2002: Advanced spectral methods for climatic time series. *Rev. Geophys.*, **40**, 1003, doi:10.1029/2000RG000092.

Golyandina, N., and A. Zhigljavsky, 2013: *Singular Spectrum Analysis for Time Series*. Springer, 120 pp.

Hannachi, A., I. T. Jolliffe, and D. B. Stephenson, 2007: Empirical orthogonal functions and related techniques in atmospheric science: A review. *Int. J. Climatol.*, **27**, 1119–1152, doi:10.1002/joc.1499.

Hirata, A., and F. E. Grimm, 2016: The role of synoptic and intraseasonal anomalies in the life cycle of summer rainfall extremes over South America. *Climate Dyn.*, **46**, 3041–3055, doi:10.1007/s00382-015-2751-6.

Hoskins, B. J., and D. J. Karoly, 1981: The steady linear responses of a spherical atmosphere to thermal and orographic forcing. *J. Atmos. Sci.*, **38**, 1179–1196, doi:10.1175/1520-0469(1981)038<1179:TSLROA>2.0.CO;2.

——, and T. Ambrizzi, 1993: Rossby wave propagation on a realistic longitudinally varying flow. *J. Atmos. Sci.*, **50**, 1661–1671, doi:10.1175/1520-0469(1993)050<1661:RWPOAR>2.0.CO;2.

Hu, T., and Q. Fu, 2007: Observed poleward expansion of the Hadley circulation since 1979. *Atmos. Chem. Phys.*, **7**, 5229–5236, doi:10.5194/acp-7-5229-2007.

Irving, D., and I. Simmonds, 2016: A new method for identifying the Pacific–South American pattern and its influence on regional climate variability. *J. Climate*, **29**, 6109–6125, doi:10.1175/JCLI-D-15-0843.1.

Jin, F. F., and B. J. Hoskins, 1995: The direct response to tropical heating in a baroclinic atmosphere. *J. Atmos. Sci.*, **52**, 307–319, doi:10.1175/1520-0469(1995)052<0307:TDRTTH>2.0.CO;2.

Karoly, D. J., 1983: Rossby wave propagation in a barotropic atmosphere. *Dyn. Atmos. Oceans*, **7**, 111–125, doi:10.1016/0377-0265(83)90013-1.

——, 1989: Southern Hemisphere circulation features associated with El Niño–Southern Oscillation events. *J. Climate*, **2**, 1239–1251, doi:10.1175/1520-0442(1989)002<1239:SHCFAW>2.0.CO;2.

Kobayashi, S., and Coauthors, 2015: The JRA-55 reanalysis: General specifications and basic characteristics. *J. Meteor. Soc. Japan*, **93**, 5–48, doi:10.2151/jmsj.2015-001.

Lau, K. M., P. J. Sheu, and I. S. Kang, 1994: Multiscale low-frequency circulation modes in the global atmosphere. *J. Atmos. Sci.*, **51**, 1169–1193, doi:10.1175/1520-0469(1994)051<1169:MLFCMI>2.0.CO;2.

Li, X., E. P. Gerber, D. M. Holland, and C. Yoo, 2015: A Rossby wave bridge from the tropical Atlantic to West Antarctica. *J. Climate*, **28**, 2256–2273, doi:10.1175/JCLI-D-14-00450.1.

Lorenz, E. N., 1956: Empirical orthogonal functions and statistical weather prediction. Tech. Rep. 1, Statistical Forecasting Project, Dept. of Meteorology, MIT, 49 pp.

Lu, J., G. A. Vecchi, and T. Reichler, 2007: Expansion of the Hadley cell under global warming. *Geophys. Res. Lett.*, **34**, L06805, doi:10.1029/2006GL028443.

——, G. Chen, and D. M. W. Frierson, 2008: Response of the zonal mean atmospheric circulation to El Niño versus global warming. *J. Climate*, **21**, 5835–5851, doi:10.1175/2008JCLI2200.1.

——, C. Deser, and T. Reichler, 2009: Cause of the widening of the tropical belt since 1958. *Geophys. Res. Lett.*, **36**, L03803, doi:10.1029/2008GL036076.

Matear, R., T. J. O'Kane, J. S. Risbey, and M. Chamberlain, 2015: Sources of heterogeneous variability and trends in Antarctic sea-ice. *Nat. Commun.*, **6**, 8656, doi:10.1038/ncomms9656.

Mo, K. C., 2000: Relationships between low-frequency variability in the Southern Hemisphere and sea surface temperature anomalies. *J. Climate*, **13**, 3599–3610, doi:10.1175/1520-0442(2000)013<3599:RBLFVI>2.0.CO;2.

——, and R. W. Higgins, 1998: The Pacific–South American modes and tropical convection during the Southern Hemisphere winter. *Mon. Wea. Rev.*, **126**, 1581–1596, doi:10.1175/1520-0493(1998)126<1581:TPSAMA>2.0.CO;2.

——, and J. N. Paegle, 2001: The Pacific South–American modes and their downstream effects. *Int. J. Climatol.*, **21**, 1211–1229, doi:10.1002/joc.685.

——, J. O. Dickey, and S. L. Marcus, 1997: Interannual fluctuations in atmospheric angular momentum simulated by the National Centers for Environmental Prediction medium range forecast. *J. Geophys. Res.*, **102**, 6703–6713, doi:10.1029/96JD02609.

Monselesan, D. P., T. J. O'Kane, J. S. Risbey, and J. Church, 2015: Internal climate memory in observations and models. *Geophys. Res. Lett.*, **42**, 1232–1242, doi:10.1002/2014GL062765.

Nguyen, H., A. Evens, C. Lucas, I. Smith, and B. Timbal, 2013: The Hadley circulation in reanalysis: Climatology, variability and change. *J. Climate*, **26**, 3357–3376, doi:10.1175/JCLI-D-12-00224.1.

O'Kane, T. J., J. S. Risbey, C. L. E. Franzke, I. Horenko, and D. P. Monselesan, 2013: Changes in the metastability of the midlatitude Southern Hemisphere circulation and the utility of nonstationary cluster analysis and split-flow blocking indices as diagnostic tools. *J. Atmos. Sci.*, **70**, 824–842, doi:10.1175/JAS-D-12-028.1.

——, ——, D. P. Monselesan, I. Horenko, and C. L. E. Franzke, 2016b: On the dynamics of persistent states and their secular trends in the waveguides of the southern hemisphere troposphere. *Climate Dyn.*, **46**, 3567–3597, doi:10.1007/s00382-015-2786-8.

Oliveira, F. N. M., L. M. V. Carvalhoc, and T. Ambrizzi, 2014: A new climatology for southern hemisphere blockings in the winter and the combined effect of ENSO and SAM phases. *Int. J. Climatol.*, **34**, 1676–1692, doi:10.1002/joc.3795.

Oort, H. A., and J. J. Yienger, 1996: Observed interannual variability in the Hadley Circulation and its connection to ENSO. *J. Climate*, **56**, 250–269.

Reid, G. C., and K. S. Gage, 1984: A relationship between the height of the tropical tropopause and the global angular momentum of the atmosphere. *Geophys. Res. Lett.*, **11**, 840–842, doi:10.1029/GL011i009p00840.

Renwick, J. A., 2005: Persistent positive anomalies in the Southern Hemisphere circulation. *Mon. Wea. Rev.*, **133**, 977–988, doi:10.1175/MWR2900.1.

——, and M. J. Revell, 1999: Blocking over the South Pacific and Rossby wave propagation. *Mon. Wea. Rev.*, **127**, 2233–2247, doi:10.1175/1520-0493(1999)127<2233:BOTSPA>2.0.CO;2.

Rogers, J. C., and H. van Loon, 1982: Spatial variability of sea level pressure and 500-mb height anomalies over the Southern Hemisphere. *Mon. Wea. Rev.*, **110**, 1375–1392, doi:10.1175/1520-0493(1982)110<1375:SVOSLP>2.0.CO;2.

Schneider, D. P., C. Deser, and Y. Okumura, 2012: An assessment and interpretation of the observed warming of West Antarctica in the austral spring. *Climate Dyn.*, **38**, 323–347, doi:10.1007/s00382-010-0985-x.

Steig, E. J., Q. Ding, D. S. Battisti, and A. Jenkins, 2012: Tropical forcing of circumpolar deep water inflow and outlet glacier thinning in the Amundsen Sea Embayment, West Antarctica. *Ann. Glaciol.*, **53**, 19–28, doi:10.3189/2012AoG60A110.

Szeredi, I., and D. J. Karoly, 1987: Horizontal structure of monthly fluctuations of the Southern Hemisphere troposphere from station data. *Aust. Meteor. Mag.*, **35**, 119–129.

Tandon, N. F., E. P. Gerber, A. H. Sobel, and L. M. Polvani, 2013: Understanding Hadley cell expansion versus contraction: Insights from simplified models and implications for recent observations. *J. Climate*, **26**, 4304–4321, doi:10.1175/JCLI-D-12-00598.1.

Thompson, D. W. J., and J. M. Wallace, 2000: Annular modes in the extratropical circulation. Part I: Month-to-month variability. *J. Climate*, **13**, 1000–1016, doi:10.1175/1520-0442(2000)013<1000:AMITEC>2.0.CO;2.

Vecchi, G. A., and B. J. Soden, 2007: Global warming and the weakening of the tropical circulation. *J. Climate*, **20**, 4316–4340, doi:10.1175/JCLI4258.1.

Wolter, K., and M. Timlin, 2011: El Niño/Southern Oscillation behaviour since 1871 as diagnosed in an extended multivariate ENSO index (MEI.ext). *Int. J. Climatol.*, **31**, 1074–1087, doi:10.1002/joc.2336.